

Reference

NBS
Publi-
cations



A11105 618701

A11101 776890

NBSIR 81-2385

Finite Difference Calculations of Buoyant Convection in an Enclosure Part I: The Basic Algorithm

Center for Applied Mathematics
Center for Fire Research

U.S. DEPARTMENT OF COMMERCE
National Bureau of Standards
Washington, DC 20234

QC 981
100
.U56
81-2385
1981

U.S. DEPARTMENT OF COMMERCE
National Bureau of Standards
National Engineering Laboratory
Center for Applied Mathematics
Washington, DC 20234

NBSIR 81-2385

JAN 25 1982

not acc - R12

Q2105

1450

NBSIR 81-2385

1981

**FINITE DIFFERENCE CALCULATIONS OF
BUOYANT CONVECTION IN AN
ENCLOSURE
PART I: THE BASIC ALGORITHM**

Howard Baum**, Ronald G. Rehm*,
P. Darcy Barnett* and Daniel M. Corley*

* Center for Applied Mathematics

**Center for Fire Research

* U.S. DEPARTMENT OF COMMERCE
National Bureau of Standards
National Engineering Laboratory
Center for Applied Mathematics
Washington, DC 20234

**U.S. DEPARTMENT OF COMMERCE
National Bureau of Standards
National Engineering Laboratory
Center for Fire Research
Washington, DC 20234

December 1981

Final Report

U.S. DEPARTMENT OF COMMERCE
National Bureau of Standards
National Engineering Laboratory
Center for Applied Mathematics
Washington, DC 20234



U.S. DEPARTMENT OF COMMERCE, Malcolm Baldrige, Secretary
NATIONAL BUREAU OF STANDARDS, Ernest Ambler, Director

10-10-10 2A-10-10-10
10-10-10 2A-10-10-10
10-10-10 2A-10-10-10

10-10-10 2A-10-10-10

Finite Difference Calculations of Buoyant
Convection in an Enclosure

Part I: The Basic Algorithm

Howard R. Baum†, Ronald G. Rehm*,
P. Darcy Barnett* and Daniel M. Corley†

National Bureau of Standards
Washington, D.C. 20234

* Center for Applied Mathematics

† Center for Fire Research



ABSTRACT

A novel mathematical model of buoyant convection in an enclosure, developed earlier, is solved by finite difference techniques in the two-dimensional case. This model has been developed as a principal analytical tool for the prediction of the movement of smoke and hot gases in fires. Effects of large density variations caused by substantial heating are retained while acoustic (high-frequency) waves, which are unimportant to buoyant convection, are analytically filtered out. No viscous or thermal conduction effects are included in the model. These two characteristics (filtering and no dissipative effects) distinguish the model from all others describing buoyant convection. The mathematical model consists of a mixed hyperbolic and elliptic set of nonlinear partial differential equations: the problem is a mixed initial, boundary value one. An explicit time-marching algorithm, second-order accurate in both space and time, is used to solve the equations. The computational procedure uses a software package for solving a nonseparable elliptic equation developed especially for this problem. The finite difference solutions have been carefully compared with analytical solutions obtained in special cases to determine the stability and accuracy of the numerical solutions. The computer model has been used to compute the buoyant convection produced in an enclosure by a spatially distributed heat source simulating a fire. The computed results show qualitative agreement with experimentally observed buoyant convection in enclosure fires.

TABLE OF CONTENTS

	<u>Page</u>
Abstract.....	i
I. Introduction.....	1
II. Formulation.....	4
A. Continuous Problem.....	4
B. Finite Difference Equations.....	12
1. Basis for the Selection of the Difference Equations.....	12
2. The Equations.....	14
III. Example Calculations.....	25
A. Square Enclosure with Centered Heat Source.....	26
B. Rectangular Enclosure with Off-Center Heat Source.....	30
Appendix.....	31
References.....	34
Figure Captions.....	36

I. Introduction

This paper presents the first results for a finite-difference integration of an approximate set of equations describing buoyant convection in an enclosure. The work represents a continuation of the research reported in Reference 1, where the set of approximate equations was derived. The primary application of interest to the authors is the movement of smoke and hot gases caused by a fire in a room.

The research presented here is distinguished from previous numerical computations of buoyant convection in three respects. First, in this model the fluid is taken to be an inviscid, non-heat-conducting perfect gas, and the spatial and temporal magnitude and variation of the heat source, which simulates a fire and drives the flow, are taken as known. These approximations are justified because under conditions characteristic of even a small room fire, the Grashof numbers (representing the ratio of the inertial to viscous forces for natural convection) are large enough for molecular transport phenomena to be important only in wall boundary layers and in the highly convoluted flame sheets which constitute the region of intense heat addition. The study of the detailed flame structure of real fires is an extraordinarily complicated subject in its own right, and is bypassed here by specifying the heat source. Wall boundary layers represent a local refinement to be considered separately at a later date. Batchelor [2] gives a brief but relevant discussion of the applicability of the inviscid equations in the context of atmospheric motions. It should be noted that such simplifications do not preclude a description of turbulence; but no turbulence model is explicitly included in this study. We note, however, that any turbulence model appended to the present equations must be of the "sub grid" variety, since no spatial or temporal averaging is

implied in the equations derived in Reference 1.

The omission of any turbulence model is based on the observation, quantified by McCaffrey [20], that most of the energy containing fluctuations in buoyant plumes induced by laboratory scale diffusion flames are of low frequency and large spatial extent. Such fluctuations, with frequencies typically in the range 2 - 5 Hz and length scales comparable to the local plume width are directly resolved by the computational procedure. A knowledge of the behavior of higher frequencies and smaller length scales is of course crucial to an understanding of combustion related phenomena. However, as noted above, such questions have been by-passed in the present study.

Simple models of smoke and hot gas transport which neglect molecular transport phenomena have been reasonably successful in predicting global properties of flow fields [3]. The present work is intended as a first step towards more detailed studies along these lines.

Second, the approximate set of equations integrated in this paper are characterized by the fact that large density variations due to temperature changes are admitted, but compressibility effects are suppressed. Such a fluid has been termed thermally expandable in other contexts [4]. In the fire setting, allowance for density variations due to temperature increases during combustion is essential. It is common for temperature in a flame to exceed 1000°C , implying that the density decreases locally to less than one-quarter its ambient value in the nearly constant-pressure process. In Reference [1], a set of equations of motion was derived formally which permit description of large density variations in a flow while ignoring acoustic oscillations arising because of the elastic properties of the fluid. Such model equations include

the important features of buoyant flows without requiring excessive computer time necessary to determine high-frequency sound waves when numerically integrated. In this sense the equations "filter out" the sound waves while describing the lower frequency, organized motions due to buoyant effects such as internal waves.

Finally, in previous efforts to compute flow fields, produced by buoyancy or by any other mechanism, there are few reported detailed checks on the quality of the numerical solutions to the finite difference equations. By contrast, in References 8 and 22 detailed comparisons are made with analytical/numerical solutions obtained to the general difference equations in simple, special cases. Through these comparisons confidence in both the algorithm and its implementation as a computer code was gained. Such tests showed that the algorithm is stable and for the example cases performed, the error made in solving the difference equations at any time step, even in the nonlinear case, was over two orders of magnitude less than the discretization errors made in approximating the partial differential equations by finite difference equations. For buoyant flows of the type considered in this paper, it is especially important to have confidence in both the stability and the accuracy of the algorithm so that the real physical instability represented by the fluid motion can be distinguished from any computational instabilities.

In Section II the equations derived in Reference 1 are recast into the form in which they are solved, and the finite difference approximations to the equations are presented. In Section III solutions determined by this model, for the buoyant flow produced by a heat source in two rectangular enclosures, are presented and discussed.

II. Formulation

A. Continuous Problem

In Reference 1 the authors derived a set of nonlinear equations describing nondissipative, buoyancy driven flows of a perfect gas. The flows were assumed to be generated by a localized heat source in which the heat is added slowly so that the time scale associated with the heat-source growth and resultant fluid motion is long compared with the transit time of an acoustic signal across the spatial extent of the source. Flows induced by a room fire generally satisfy this assumption. Properties of the equations were discussed in Reference 1. In this section these equations are rewritten in a form appropriate for numerical integration by finite difference techniques, and the boundary conditions for the equations are presented.

As in Reference 1 we consider an inviscid, non-heat-conducting perfect gas. The magnitude and the spatial variation of the heat source (representing the exothermic reaction in a fire) are taken as known; justification for such a model is given in Reference 1. The fluid and the fire source are assumed confined in a closed rectangular room with the center of the source along the floor. In contrast to Reference 1, we consider only a completely enclosed room (no leaks), and when difference equations are introduced, we confine attention to the two dimensional evolution of the flow.

The continuity, momentum, energy, and state equations are given respectively in Reference 1 as:

$$\frac{\partial \rho}{\partial t} + \frac{\partial}{\partial x_i} (\rho u_i) = 0$$

$$\rho \left(\frac{\partial u_i}{\partial t} + u_j \frac{\partial u_i}{\partial x_j} \right) + \frac{\partial (p - p_0(t))}{\partial x_i} - \rho k_i g = 0 \quad (1)$$

$$\rho c_p \left(\frac{\partial T}{\partial t} + u_j \frac{\partial T}{\partial x_j} \right) - \frac{dp_0}{dt} = Q(x_i, t)$$

$$p_0(t) = \rho RT$$

Here ρ is density, u_i the velocity in the i^{th} coordinate direction ($i = 1, 2, 3$), p is the pressure excess above the mean pressure $p_0(t)$ in the room, T the temperature, c_p the constant-pressure specific heat, R the gas constant, $k_i g$ is the gravitational acceleration (of magnitude g) and $Q(x_i, t)$ the specified volumetric heat source. The spatially uniform mean pressure $p_0(t)$ depends only upon time and increases because of the heating within the the room. It is determined in a completely enclosed room by the equation

$$\frac{dp_0}{dt} = \frac{\gamma - 1}{V} \int_V Q(x_i, t) dV \quad (2)$$

where γ is the ratio of specific heats, V is the volume of the room and the integration is performed over this entire volume. Equation (2) is a thermodynamic statement that the mean pressure rise as a function of time is determined by the total heat added to the room. (Heat can only be added or removed volumetrically and not through the walls because thermal conduction and radiative transport have been ignored in this model.) It will also turn out to be a mathematical consistency condition required if a solution for the pressure field is to exist.

Equations (1) and (2), are the approximate set of nonlinear equations solved by finite difference techniques in two spatial dimensions in this paper. The equations admit buoyant or internal-wave motions while "filtering out" high-frequency, acoustic waves. They reduce to the Boussinesq equations when heating is mild, total density variations are small, and variations in the mean background pressure can be neglected (as would be the case if the room considered here were open or if the mean pressure variation were comparable to the spatial pressure perturbation). To recast the equations into a form more suitable for numerical computation, we take the substantial derivative of the equation of state and use this with the energy equation to eliminate the temperature. The resulting equation describes the evolution of the density under heating

$$\frac{\partial \rho}{\partial t} + u_i \frac{\partial \rho}{\partial x_i} = - \rho \frac{\partial u_i}{\partial x_i} = - \rho D(x_j, t) \quad (3)$$

where

$$D(x_j, t) = \frac{1}{\gamma p_0(t)} \left[(\gamma - 1) Q(x_j, t) - \frac{dp_0}{dt} \right] \quad (4)$$

Equation (3) and the continuity equation identify $D(x_i, t)$ as the divergence

$$\frac{\partial u_i}{\partial x_i} = D(x_j, t) \quad (5)$$

Finally, as in Reference 1, the equation for the spatially variable portion of the pressure is obtained by dividing the momentum equations by density and taking the divergence of these equations. The resulting equation is

$$\frac{\partial}{\partial x_i} \left(\frac{1}{\rho} \frac{\partial p}{\partial x_i} \right) = - \left[\frac{\partial}{\partial x_i} \left(u_j \frac{\partial u_i}{\partial x_j} \right) + \frac{\partial D(x_j, t)}{\partial t} \right] \quad (6)$$

Equation (6) is the generalization for a "thermally expandable" fluid, which we consider here, of the well-known incompressibility condition in Boussinesq fluids. When the density is constant, then $D(\vec{x}, t) = 0$, and Equation (6) reduces to Poisson's equation. The boundary conditions on these equations are that velocity normal to any (impermeable) wall vanish.

$$u_i n_i = 0 \quad (7)$$

where n_i are the normal components of a vector describing the boundary walls. From Equations (1) and these conditions, the appropriate boundary conditions on the pressure equation are obtained

$$n_i \frac{\partial p}{\partial n_i} = \rho g \quad n_i k_i \quad (8)$$

An important observation must be made concerning Equation (6) and Neumann boundary conditions (8). When Equation (6) is integrated over the total volume of the room, both the left hand side of the equation and the first term on the right are divergence forms and can be converted into integrals over the boundaries of the room. Application of boundary conditions (7) and (8) show that each of the terms is zero; therefore, the integral over the volume of $\frac{\partial D}{\partial t}$ must also be zero. The requirement that the integral of Equation (4) for D over the volume be zero produces Equation (2), the condition for the spatially uniform background pressure. Therefore, the elliptic equation, Equation (6), for the pressure, with the Neumann boundary conditions, is seen to produce a condition which must be satisfied for a solution to the equation to exist. This condition, Equation (2), determines the time evolution of the spatially uniform background pressure and demonstrates that the total pressure can be consistently separated into a spatially uniform background pressure and an

inhomogeneous time dependent over-pressure. In the next section describing the difference equations, exactly analogous considerations are found to apply to the linear algebraic equations approximating Equation (6) and boundary conditions (8).

For selecting a difference scheme, the second of Equations (1), the momentum equations, are rewritten in vector invariant form, noting that u_i are components of the velocity vector field \vec{u}

$$\frac{\partial \vec{u}}{\partial t} + 1/2 \nabla (q^2) - \vec{u} \times \vec{\omega} = - \frac{1}{\rho} \nabla p + \vec{k} g \quad (9)$$

where $q^2 = \vec{u} \cdot \vec{u}$ and $\vec{\omega} = \nabla \times \vec{u}$ is the vorticity. The curl of Equation (9) yields the vorticity-transport equation

$$\frac{\partial \vec{\omega}}{\partial t} - \nabla \times (\vec{u} \times \vec{\omega}) = - \nabla \left(\frac{1}{\rho} \right) \times \nabla p \quad (10)$$

Since \vec{u} is a vector field, it is necessary to calculate correctly both its divergence and its curl. Equation (5) specifies the divergence of \vec{u} , and the equation for the pressure, Equation (6), assures that the divergence is properly determined at each time. Equation (10) is the equation for the evolution of the curl of the velocity, the vorticity. The difference scheme selected must assure that Equation (10) is satisfied in difference form.

The complete set of recast nonlinear equations are gathered and rewritten

below.

$$\frac{\partial \rho}{\partial t} + u_i \frac{\partial \rho}{\partial x_i} = - \rho D(x_j, t) \quad (11a)$$

$$\frac{\partial u_i}{\partial t} + 1/2 \frac{\partial}{\partial x_i} (u_j u_j) - \epsilon_{ijl} u_j \omega_l = - \frac{1}{\rho} \frac{\partial p}{\partial x_i} + k_i g \quad (11b)$$

$$\frac{\partial}{\partial x_i} \left(\frac{1}{\rho} \frac{\partial p}{\partial x_i} \right) = - \left[\frac{\partial}{\partial x_i} \left(u_j \frac{\partial u_i}{\partial x_j} \right) + \frac{\partial D(x_j, t)}{\partial t} \right] \quad (11c)$$

where

$$\frac{dp_0}{dt} = \frac{\gamma-1}{V} \int_V Q(x_i, t) dV \quad (11d)$$

$$D(x_i, t) = \frac{1}{\gamma p_0(t)} \left[(\gamma-1) Q(x_i, t) - \frac{dp_0}{dt} \right] \quad (11e)$$

ϵ_{ijl} is the permutation tensor and

$\omega_i = \epsilon_{ijl} \frac{\partial u_l}{\partial x_j}$ are the components of the vorticity vector.

Boundary conditions are

$$u_i n_i = 0 \quad (12a)$$

$$n_i \frac{\partial p}{\partial x_i} = \rho g k_i n_i \quad (12b)$$

For numerical integration, Equations (11) and boundary conditions (12) are altered in two additional ways. First, we calculate the density and pressure differences from their initial values, which may be functions of the vertical coordinate. This is done to eliminate accuracy problems, since the thermally induced density and pressure differences can be very small during the early portion of the heating process. Second, the equations are made dimensionless. The nondimensionalization is done both for convenience and to ensure proper scaling. All dependent quantities are made to be of order unity in magnitude for purposes of the computation. The remaining dimensionless parameters characterize the strength and location of the heat source as well as the room geometry.

In Figure 1 a schematic diagram of a fire evolving a room and a set of coordinate axes are shown. It is assumed that initially the enclosure is filled with quiescent, stratified fluid of density $\rho_0(y)$, where we denote $x_1 = x$, $x_2 = y$ and $x_3 = z$. We define a density difference from ambient and a pressure difference as follows:

$$\tilde{\rho}(x, y, z, t) = \rho(x, y, z, t) - \rho_0(y) \quad (13a)$$

$$\tilde{p}(x, y, z, t) = p(x, y, z, t) - p_0(t) + g \int_0^y \rho_0(y') dy' \quad (13b)$$

These differences $\tilde{\rho}$ and \tilde{p} need not be small compared with $\rho_0(y)$ and $p_0(t)$ respectively. Then Equations (11a)–(11c) become

$$\frac{\partial \tilde{\rho}}{\partial t} + u_1 \frac{\partial \tilde{\rho}}{\partial x_1} + v \frac{d\rho_0}{dy} = -(\rho_0(y) + \tilde{\rho}) D(x_j, t) \quad (14a)$$

$$\frac{\partial u_i}{\partial t} + 1/2 \frac{\partial}{\partial x_i} (u_j u_j) - \epsilon_{ijl} u_j \omega_l = - (1/(\rho_o + \tilde{\rho})) \left[\frac{\partial p}{\partial x_i} - k_i g \tilde{\rho} \right] \quad (14b)$$

$$\left(\frac{\partial}{\partial x_i} (1/(\rho_o + \tilde{\rho})) \frac{\partial \tilde{p}}{\partial x_i} \right) = - \left[\frac{\partial}{\partial y} (g \tilde{\rho}/(\rho_o + \tilde{\rho})) + \frac{\partial D}{\partial t} + 1/2 \frac{\partial^2}{\partial x_i^2} (q^2) - \frac{\partial}{\partial x_i} \epsilon_{ijl} u_j \omega_l \right] \quad (14c)$$

where $v = u_2$ and $q^2 = u_i u_i$

and the boundary condition (12b) becomes

$$n_i \frac{\partial \tilde{p}}{\partial x_i} = \rho g k_i n_i \quad (15)$$

Finally, we form dimensionless equations using the density $\rho_{oo} \equiv \rho_o(0)$, the height of the room H as the length scale and the free fall time $(H/g)^{1/2}$ as the time scale. Then, denoting dimensionless quantities with a hat

$$\begin{aligned} \hat{\rho} &= \tilde{\rho}/\rho_{oo} \quad , \quad \hat{p} = \tilde{p}/\rho_{oo} g H \quad , \quad \hat{\rho}_o = \rho_o/\rho_{oo} \\ \hat{u}_i &= u_i/\sqrt{gH} \quad , \quad \hat{x}_i = x_i/H \quad , \quad \hat{t} = t/\sqrt{(H/g)} \end{aligned} \quad (16)$$

Equations (13) remain exactly the same in dimensionless form with g set equal to one. Subsequently, in this paper all quantities will be understood to be dimensionless, and the hat notation will be dropped. For the dimensionless coordinates, we note that $0 \leq x \leq 1/AR$, $0 \leq y \leq 1$ and $0 \leq z \leq 1/BR$ where $AR \equiv H/L$ and $BR \equiv H/W$. Also, in the remainder of this paper, the problem will be specialized to two spatial dimensions so that all quantities will be assumed independent of z .

This non-dimensionalization, while simplifying the form of the equations, does not relate the scale of the induced motion to that of the source. An alternative scheme which does have this feature is derived in the Appendix. The resulting equations are somewhat less convenient for numerical computation, except in the Boussinesq limit when density differences are small. Hence, the variables as defined by Equation (16) will be used throughout the remainder of the paper.

B. Finite Difference Equations

1. Basis for the Selection of the Difference Equations

In this section the finite difference equations and the boundary relations for the solution-algorithm are presented. This algorithm does not represent a new numerical scheme; rather it represents an adaptation of several well-known and proven ideas to the equations of interest here. Since these equations are different than those generally examined in computational fluid dynamics, there are interesting features which will be noted as the difference equations are presented.

It is important first, however, to state the requirements which we used in selecting the scheme. These requirements do not necessarily specify a unique scheme, but restrict greatly the selection. As noted in the previous subsection, the momentum conservation equations provide relations for determining the velocity field, which is a vector field, as a function of time. Forming the difference equations from the vector invariant form of the momentum equations is one criterion. This choice is made to assure that, when the discrete analogues of the divergence and curl are applied to the difference equations,

suitable discretized equations for the pressure and the vorticity transport are obtained. Thus we can be certain that the divergence and the curl are calculated correctly in discrete form, the divergence producing the equation for the pressure and the curl producing an evolution equation for vorticity.

A second criterion imposed is that the difference equations provide second-order-accurate approximations to the partial differential equations. This condition is imposed because second order accuracy is necessary to obtain reasonable spatial and temporal resolution for the hundreds of time steps required to calculate the complete evolution of the flow field in a room fire.

A well-understood buoyant flow field is that produced by internal waves in an ambient stratified environment. Internal waves have been analyzed and calculated for a long time [6,7]; they are determined as solutions to the linearized partial differential equations of buoyant flow. In addition, internal waves can be expected to arise naturally in a room fire setting when the driving fire has heated and stratified the room air; after the fire has extinguished itself because of vitiated air, for example, pure internal wave modes will exist. An additional criterion which was imposed on the selection of the difference scheme was that it accurately reproduce internal-wave modes in an enclosure: if the difference scheme does not reproduce this rather simple linear flow field, it is unlikely to reproduce more complicated flows. In Reference 8 the authors examined internal waves and some second order linear difference equations that reproduce these waves. This analysis determined the difference scheme for all but the non-linear convective terms in the momentum equations.

In an important paper for numerical weather forecasting [9], Arakawa discusses design of computational schemes for long-term numerical integration of the equations of fluid motion in the case of two-dimensional incompressible flow. The major thrust of his paper is a derivation of second-order accurate spatial difference schemes which eliminate the nonlinear computational instability first noted by Phillips [10]. Arakawa emphasizes that for two-dimensional, incompressible flow, the discrete approximations to quadratic forms of dependent variables, such as the velocity squared or the vorticity squared (or both), must be conserved when the continuous variables are, and he uses this constraint to select three difference approximations which are acceptable. Another criterion imposed in the selection of our difference scheme is that it reduce to one of Arakawa's acceptable, or stable schemes with respect to the nonlinear computational instability when the flow is incompressible. The scheme chosen is denoted J_3 by Arakawa [11] and conserves energy in the incompressible case. It can be obtained by differencing the vector invariant form of the momentum equations.

Finally, we wanted the difference scheme to be easily generalized to three-dimensional flow configurations. For a model of buoyant flow driven by a fire to be successful, it must be able to calculate three-dimensional flows. The scheme selected and presented below satisfies all of the criteria stated above.

2. The Equations

In Figure 2a, the two-dimensional rectangular enclosure in dimensionless

variables is shown together with a schematic representation of the spatial grids used for the finite difference scheme. The grid formed from solid lines represents the basic mesh into which the enclosure is divided: in general there are I mesh cells in the x-direction and J mesh cells in the y-direction. Upon this basic mesh, the two components of the vector velocity (u, v) and single surviving component of the vector vorticity $\omega = \frac{\partial v}{\partial x} - \frac{\partial u}{\partial y}$ are defined.

The second grid, formed by joining the center points of the basic grid cells and denoted by dashed lines, is that upon which scalar quantities such as density ρ and pressure p are defined. In Figure 2a the densities in the left-hand column of cells and in the bottom row of cells are shown to indicate how they are enumerated for the numerical computation.

In Figure 2b a typical mesh cell is shown, illustrating where all of the dependent variables in the finite difference scheme are defined relative to the cell.

The following discretely evaluated functions will denote approximations to the corresponding solutions to Equations (9) and (10):

$$u_{ij}^n \cong u(i\delta x, (j-1/2)\delta y, n\delta t)$$

$$v_{ij}^n \cong ((i-1/2)\delta x, j\delta y, n\delta t)$$

$$\rho_{ij}^n \cong \rho((i-1/2)\delta x, (j-1/2)\delta y, n\delta t)$$

$$p_{ij}^n \cong p((i-1/2)\delta x, (j-1/2)\delta y, n\delta t)$$

$$D_{ij}^n = D((i-1/2)\delta x, (j-1/2)\delta y, n\delta t) ,$$

$$\omega_{ij}^n \cong \omega(i\delta x, j\delta y, n\delta t)$$

where $\delta x = 1/(I \cdot AR)$ and $\delta y = 1/J$ are the mesh cell sizes in the x- and y-directions respectively and where δt is the time-step size. Such a staggered grid is commonly used for multidimensional finite difference integrations [12].

With this notation, the following set of finite difference equations was used to approximate Equations (11) and boundary conditions (12):

For Equation (14a), $1 \leq i \leq I$, $1 \leq j \leq J$ and $n \geq 2$,

$$\rho_{ij}^{n+1} = \frac{1}{1 + (1/2)D_{ij}^n \delta t} \left\{ \rho_{ij}^{n-1} \left(1 - (1/2)D_{ij}^n \delta t \right) \right. \quad (18)$$

$$\left. - 2\delta t \left(F_{\rho x ij}^n + F_{\rho y ij}^n + (1/2)D_{ij}^n \rho_o(j) \right) \right\}$$

where

$$\rho_{ij}^n = \rho_{ij}^n - \rho_o(j) = \text{the density difference from the initial density,}$$

$$\rho_o(j) = \exp[-(j-1/2)\delta y/Y_s] = \text{the prescribed ambient initial stratification,}$$

(19)

Y_s = the stratification length scale.

The flux terms $F_{\rho x_{ij}}^n$ and $F_{\rho y_{ij}}^n$ for $1 \leq i \leq I$, $1 \leq j \leq J$ are given by

$$F_{\rho x_{ij}}^n = \left(\frac{2\rho_o(j) + \rho_{i+1,j}^{\sim n} + \rho_{i-1,j}^{\sim n}}{4} \right) \left(\frac{u_{ij}^n - u_{i-1,j}^n}{\delta x} \right) + \left(\frac{\rho_{i+1,j}^{\sim n} - \rho_{i-1,j}^{\sim n}}{2\delta x} \right) \left(\frac{u_{ij}^n + u_{i-1,j}^n}{2} \right) \quad (20a)$$

$$F_{\rho y_{ij}}^n = \left(\frac{\rho_o(j+1) + \rho_o(j-1) + \rho_{i,j+1}^{\sim n} + \rho_{i,j-1}^{\sim n}}{4} \right) \left(\frac{v_{ij}^n - v_{i,j-1}^n}{\delta y} \right) + \left(\frac{\rho_o(j+1) - \rho_o(j-1) + \rho_{i,j+1}^{\sim n} - \rho_{i,j-1}^{\sim n}}{2\delta y} \right) \left(\frac{v_{ij}^n + v_{i,j-1}^n}{2} \right) \quad (20b)$$

Equation (18) employs a modification of the second-order accurate central difference (leap frog) temporal discretization. The modification eliminates an instability that would arise if the leap frog scheme had been applied. It affects the undifferentiated term $\tilde{\rho}D(x,y,t)$ in equation (14) that is well known to lead to a computational instability for ordinary differential equations when leap frog differencing is used [13].

For Equations (14b)

$$u_{ij}^{n+1} = u_{ij}^{n-1} - 2\delta t \left\{ F_{x_{ij}}^n + \frac{2}{\delta x} \left(\frac{\rho_{i+1,j}^{\sim n} - \rho_{ij}^{\sim n}}{2\rho_o(j) + \rho_{i+1,j}^{\sim n} + \rho_{ij}^{\sim n}} \right) \right\} \quad (21a)$$

and for $1 \leq i \leq I-1$, $1 \leq j \leq J$,

$$v_{ij}^{n+1} = v_{ij}^{n-1} - 2\delta t \left\{ F_{yij}^n + \frac{2}{\delta y} \left(\frac{\tilde{p}_{i,j+1}^n - \tilde{p}_{ij}^n + \left(\tilde{\rho}_{i,j+1}^n + \tilde{\rho}_{ij}^n \right) \frac{\delta y}{2}}{\rho_0(j+1) + \rho_0(j) + \tilde{\rho}_{i,j+1}^n + \tilde{\rho}_{ij}^n} \right) \right\} \quad (21b)$$

for $1 \leq i \leq I$, $1 \leq j \leq J-1$.

The fluxes F_{xij}^n and F_{yij}^n are defined as follows:

for $1 \leq i \leq I-1$, $1 \leq j \leq J$

$$F_{xij}^n = \frac{1}{2\delta x} \left[\left(q_{i+1,j}^n \right)^2 - \left(q_{ij}^n \right)^2 \right] - \frac{1}{2} \left(v_{\omega_{ij}}^n \omega_{ij}^n + v_{\omega_{i,j-1}}^n \omega_{i,j-1}^n \right) \quad (22a)$$

and for $1 \leq j \leq J-1$, $1 \leq i \leq I$

$$F_{yij}^n = \frac{1}{2\delta y} \left[\left(q_{i,j+1}^n \right)^2 - \left(q_{ij}^n \right)^2 \right] + \frac{1}{2} \left(u_{\omega_{ij}}^n \omega_{ij}^n + u_{\omega_{i-1,j}}^n \omega_{i-1,j}^n \right) \quad (22b)$$

and where

$$\omega_{ij}^n = \frac{v_{i+1,j}^n - v_{ij}^n}{\delta x} - \frac{u_{i,j+1}^n - u_{ij}^n}{\delta y}$$

$$v_{\omega_{ij}}^n = \frac{1}{2} (v_{ij}^n + v_{i+1,j}^n), \quad u_{\omega_{ij}}^n = \frac{1}{2} (u_{i,j+1}^n + u_{ij}^n) \quad (22c)$$

$$\left(q_{ij}^n \right)^2 = \left(\frac{u_{ij}^n + u_{i-1,j}^n}{2} \right)^2 + \left(\frac{v_{ij}^n + v_{i,j-1}^n}{2} \right)^2$$

Note that boundary conditions (12a) on the normal velocities imply that

$u_{0,j} = u_{I,j} = 0$ for $1 \leq j \leq J$ and $v_{i,0} = v_{i,J} = 0$ for $1 \leq i \leq I$. These boundary conditions are applied formally in the expressions for the fluxes $F_{\rho x ij}^n$, $F_{\rho y ij}^n$,

$F_{x ij}^n$ and $F_{y ij}^n$ in mesh cells adjacent to boundaries.

The finite difference analog to Eq. (14C) is, for $1 \leq i \leq I$ and $1 \leq j \leq J$

$$\begin{aligned}
 & \frac{2}{\delta x^2} \left[\frac{\tilde{p}_{i+1,j}^n - \tilde{p}_{ij}^n}{2\rho_o(j) + \rho_{i+1,j}^n + \rho_{ij}^n} - \frac{\tilde{p}_{ij}^n - \tilde{p}_{i-1,j}^n}{2\rho_o(j) + \rho_{ij}^n + \rho_{i-1,j}^n} \right] \\
 & + \frac{2}{\delta y^2} \left[\frac{\tilde{p}_{i,j+1}^n - \tilde{p}_{ij}^n}{\rho_o(j+1) + \rho_o(j) + \rho_{i,j+1}^n + \rho_{ij}^n} - \frac{\tilde{p}_{ij}^n - \tilde{p}_{i,j-1}^n}{\rho_o(j) + \rho_o(j-1) + \rho_{ij}^n + \rho_{i,j-1}^n} \right] \\
 & = - \frac{D_{ij}^{n+1} - D_{ij}^{n-1}}{2\delta t} + \frac{F_{x,i-1,j}^n - F_{x,ij}^n}{\delta x} + \frac{F_{y,i,j-1}^n - F_{y,ij}^n}{\delta y} \\
 & - \frac{1}{\delta y} \left[\frac{\tilde{\rho}_{i,j+1}^n + \tilde{\rho}_{ij}^n}{\rho_o(j+1) + \rho_o(j) + \rho_{i,j+1}^n + \rho_{ij}^n} - \frac{\tilde{\rho}_{ij}^n + \tilde{\rho}_{i,j-1}^n}{\rho_o(j) + \rho_o(j-1) + \rho_{ij}^n + \rho_{i,j-1}^n} \right] \quad (24)
 \end{aligned}$$

This difference equation for the pressure arises formally by applying the finite difference analogue of the divergence operator to Equation (21) and noting that the finite difference divergence of the velocity field satisfies the equation

$$\frac{u_{ij}^n - u_{i-1,j}^n}{\delta x} + \frac{v_{ij}^n - v_{i,j-1}^n}{\delta y} = D_{ij}^n \quad (25)$$

(This equation is the difference approximation to Equation (5).)

The boundary conditions (15) in discrete form become

$$\begin{aligned} \tilde{p}_{0,j}^n &= \tilde{p}_{1,j}^n \\ &\text{for } 1 \leq j \leq J \end{aligned} \quad (26a)$$

$$\begin{aligned} \tilde{p}_{I,j}^n &= \tilde{p}_{I+1,j}^n \\ \tilde{p}_{i,1}^n - \tilde{p}_{i,0}^n &= \delta y \left(\tilde{\rho}_{i,1}^n + \tilde{\rho}_{i,0}^n \right) / 2 \\ &\text{for } 1 \leq i \leq I \end{aligned} \quad (26b)$$

Although $\tilde{\rho}_{i,0}^n$ and $\tilde{\rho}_{i,J+1}^n$ appear in the boundary conditions, Equation 26(b), they also appear in Equation (24) with $j = 1, J$ in the same combination. As a result, $\tilde{\rho}_{i,0}^n$ and $\tilde{\rho}_{i,J+1}^n$ never need to be specified to obtain a solution to

Equation (24) and the boundary conditons (26). Equations (24) together with boundary conditions (26) constitute a singular linear algebraic system of equations. When Equations (24), with boundary conditions (26) incorporated, are summed, the left hand side sums to zero, demonstrating that all of the equations are not linearly independent. Also, the last three terms on the right hand side sum to zero, producing the requirement that the double sum

over $\frac{D_{ij}^{n+1} - D_{ij}^{n-1}}{2\delta t}$ must vanish.

The vanishing of the sum of the left hand sides of Eqs. (24) and (26) is the discrete analog of the fact that the left hand side of the integral of Eq. (6) over the room volume vanishes when the boundary conditions $\vec{u} \cdot \vec{n} = 0$ are applied. The vanishing of the sum of the right hand sides of Eqs. (24) and (26) is the corresponding discrete analog for the requirement on the integral of the right hand side of Equation (6). This requirement, that $\sum \sum D_{ij}$ must vanish at each time level, is the discrete analog of Eq. (11d).

Examination of Equation (28) for D_{ij}^n shows that it has been chosen so that its double sum over all mesh points vanishes, and that the condition which must be satisfied to allow this choice produces Equation (29) for the mean pressure. Therefore, the singular linear algebraic system is seen to be consistent and thus to allow a solution. The solution is made unique by specifying that the double sum over all mesh points of \tilde{p}_{ij}^n is zero. This is tantamount to specifying that P_0 is literally the mean pressure in the room, with \tilde{p}_{ij}^n the perturbation about the mean. Details of the algorithm used to solve Equations (24) and (26) for \tilde{p}_{ij}^n are presented in Reference 17.

The heat source has been chosen to have the form

$$Q_{ij}^n = \hat{Q}_{ij}^n f^n \quad (27a)$$

$$\hat{Q}_{ij}^n = \left(\frac{\beta}{\pi}\right)^{1/2} \lambda \exp [-\beta(x_i - x_c)^2 - \lambda y_j] \quad (27b)$$

$$x_i = (i-1/2)\delta x, \quad y_j = (j-1/2)\delta y \quad (27c)$$

$$f^n = Q_0 \tanh At^n \quad (27d)$$

$$t^0 = 0, \quad t^n = \sum_{n'=0}^{n-1} \delta t^{n'} \quad (27e)$$

Hence, the discrete divergence of the velocity field becomes

$$D_{ij}^n = \frac{1}{\gamma p_o^n} [(\gamma-1)\hat{Q}_{ij}^n - K] f^n \quad (28a)$$

where

$$K = \frac{\gamma-1}{IJ} \sum_{i=1}^I \sum_{j=1}^J \hat{Q}_{ij} \quad (28b)$$

and the mean background pressure is found from the difference equation

$$p_o^{n+1} = p_o^{n-1} + K f^n \delta t^n \quad (29)$$

with $p_o^0 = p_o^1 = 1$ since $f^0 = 0$.

Since difference equations (18) and (21) are three-level, second-order schemes (leap-frog) in time, a starting procedure is needed. The following first-order, explicit scheme was used to start the computation and to restart when a change in the time step has been made:

$$u_{ij}^{n+1} = u_{ij}^n - \delta t \left\{ F_{xij}^n + \frac{2}{\delta x} \left(\frac{\tilde{p}_{i+1,j}^n - p_{ij}^n}{2\rho_o(j) + \rho_{i+1,j}^n + \rho_{ij}^n} \right) \right\} \quad (30a)$$

$$v_{ij}^{n+1} = v_{ij}^n - \delta t \left\{ F_{yij}^n + \frac{2}{\delta y} \left(\frac{\tilde{p}_{i,j+1}^n - p_{ij}^n + \left(\frac{\tilde{p}_{i,j+1}^n}{\rho_{i,j+1}^n} + \frac{\tilde{p}_{ij}^n}{\rho_{ij}^n} \right) \frac{\delta y}{2}}{\rho_o(j+1) + \rho_o(j) + \rho_{i,j+1}^n + \rho_{ij}^n} \right) \right\} \quad (30b)$$

$$\rho_{ij}^{n+1} = \rho_{ij}^n - \delta t \left\{ (1/2) \left[\rho_o(j) + \rho_{ij}^n \right] \left[D_{ij}^n + F_{\rho xij}^n + F_{\rho yij}^n \right] \right\} \quad (31a)$$

$$p_o^{n+1} = p_o^n + Kf^n \delta t \quad (31b)$$

When starting, Equations (31) are used to obtain p_o^{n+1} and ρ_{ij}^{n+1} . Then p_{ij}^n

is obtained from Equation (24) with $\frac{D_{ij}^{n+1} - D_{ij}^{n-1}}{2\delta t}$ replaced by $\frac{D_{ij}^{n+1} - D_{ij}^n}{\delta t}$.

With this solution for \tilde{p}_{ij}^n , Equations (30) are used to obtain u_{ij}^{n+1} and v_{ij}^{n+1} . The starting procedure is completed (and two levels of all dependent variables have been obtained) by solving Equation (24) with n replaced by $n+1$ throughout. Subsequent time steps are taken in a straightforward fashion with the density and velocity components being advanced through Equations (18) and (21), and the pressure being updated through Equation (24).

The linear stability of the algorithm is the only other consideration for discussion. A linear stability analysis of Equation (18) for the density shows that the time step δt must satisfy the following condition for stability

$$\delta t \leq \max_{\substack{1 \leq i \leq I \\ 1 \leq j \leq J}} \left\{ \left(D_{ij}^n \right)^2 + \left[\frac{|U_{ij}^n|}{\delta x} + \frac{|V_{ij}^n|}{\delta y} \right]^2 \right\}^{-1/2} \quad (32)$$

where $U_{ij}^n \equiv (1/2) \left(u_{ij}^n + u_{i-1,j}^n \right)$

$$V_{ij}^n \equiv (1/2) \left(v_{ij}^n + v_{i,j-1}^n \right)$$

When the stability condition, Equation (32), is not satisfied by a time step, the time step δt^n is halved. Then the time-marching algorithm is restarted using the last time-level values as initial conditions. A first-order time step is taken and then leap frog is resumed.

When the finite difference analogue of the curl (see Equations (22)) is applied to the difference equations for the velocity components, Equations (21), a discretized form of the equation for the vorticity transport, Equation (10), is formed. A linear stability analysis of the difference equation yields exactly the same form for the stability criterion as that found above for the density equation. Reference to Figure 2b shows that the density and vorticity are evaluated at different points in the mesh, however, and therefore, the divergence D and the velocity components U and V are to be evaluated at different points than those used in Equation (32). To account for the difference in the stability criterion implied by the different mesh location points, in all calculations performed using the algorithm described above, the time step was chosen to be less than or equal to 0.8 the maximum value found for the right hand side of Equation (32).

III. Example Calculations

The algorithm, described in Section II and tested as discussed in Reference 22, has been used to compute solutions to the buoyant-flow equations. In this section results of two computations are presented and discussed. One calculation is for the flow generated by a heat source centered along the floor in a square enclosure, and the other is for the flow generated by a heat source with maximum along the floor, but off-center in a rectangular enclosure, twice as long as it is high. Other calculations, exploring parametrically the features of this model and examining in detail the numerical results by analyzing the flow data computed by the model, will be reported in a companion paper.

A. Square Enclosure with Centered Heat Source

In Figure 3 contours of constant temperature (isotherms) are shown at dimensionless time 2.0 for a volumetric heat source centered along the floor in a square room. The rate of heat added per unit volume is largest along the floor at the center of the room and decreases in a Gaussian fashion with horizontal distance from the center and exponentially with height above the floor: the dependence of the heat source upon position in the room is given by Equation (27) with $x_c = 0.5$. The heat source is "turned on" slowly according to Equations (27a) and (27d) asymptoting to full strength around $t = 10.0$. At this early time the problem is still linear; the flow velocities are sufficiently small that convection is unimportant, and the temperature increase in the fluid is directly proportional to the volumetric rate of heat added. Therefore, the isotherms are also contours along which the volumetric heat-addition rate is constant. (These contours can be seen to be parabolas by examination of Equation (27b), which describes the spatial dependence of the heat source selected for these computations.) These computations were performed on a spatial mesh of $I = J = 31$; the tick marks along the boundary of the enclosure show the mesh cell spacing.

In Figure 4 isotherms at dimensionless time $t = 10.0$ are shown. By this time the flow-field is nonlinear, and the temperature profiles are severely distorted due to buoyancy effects. The temperature has increased and the density has decreased where heating has occurred. The heated fluid has become lighter than its surrounding and begins to rise due to buoyancy. By continuity, surrounding fluid begins to be drawn into the region of the heat source, and the

isotherms, therefore, appear to be pinched off at the bottom (near the center of the heat source). Two vortices of equal and opposite strength located on the two halves of the heat source have developed to the size where their combined flow field is significant.

At time 11.5, Figure 5, a buoyant thermal has developed, giving the appearance of a mushroom cloud. The two vortices mentioned above have begun to rise with the fluid, being convected out of the region of primary heating. The buoyant thermal intensifies in strength as shown in the next two plots at times 12.5 and 13.5, Figures 6 and 7, until the thermal hits the ceiling, as shown in Figure 8, time 14.5, and begins to spread. Inside the plume a distinctly periodic structure has begun to develop, as can be seen vividly in Figure 7; here, progressing up the plume along its centerline, one finds a local low first, then a periodic sequence of local highs and lows up to about the center of the head of the thermal.

The heated gases are seen to spread along the ceiling in Figure 9 (time 15.5) and fill the room from the top down, as shown in Figures 10, 11, and 12. This physical behavior is exactly what is observed in room-fire tests and in other experimental observations of heating in enclosures. The symmetry about the centerline of the room displayed in these computations is some measure of the accuracy with which they were performed: the heat source is placed symmetrically, but the computations were performed as if no symmetry existed.

To assess the resolution of the computed results shown in Figures 3-12, the flow field was computed again using a larger number of mesh points $I = 63$, $J = 64$. Selected plots from this larger computation are shown in Figures 13-18.

These plots demonstrate that the large-scale features determined by the 31×31 computation are correct and agree with those determined from the larger computation to within about ten percent. The results from the larger computation are characterized by smoother isotherms and more detailed structures because of the greater resolution. We note that the time required for the buoyant thermal to reach the ceiling is about ten percent longer in the 63×64 results than in the 31×31 results, again apparently because of the greater spatial (and temporal) resolution of the larger computation.

Detail on a length scale of the order of one or two mesh cells must be disregarded because the computations cannot resolve such detail. On the other hand, features with a larger length scale can be interpreted. The spatially periodic behavior in the plume noted above is a feature which requires some discussion. The starting thermal and the plume induced by a heat source in an enclosure are a result of physical instability of the flow field. In addition, in the introduction, we discussed the fact that this fluid model was one in which viscosity has been ignored, and, therefore, it could be considered to result from the Navier-Stokes equations in the limit of very large Grashof number (roughly Reynolds number squared).

Over the last several years, starting with the pioneering work of Brown and Roshko,¹⁸ there has been a reexamination of the meaning of turbulence in shear flows. There had been a growing realization that turbulence is not satisfactorily described in terms of velocity correlations and their corresponding spectra only. Rather there are distinct coherent vortex structures in shear flows, and Brown and Roshko vividly demonstrated the existence of these coher-

ent structures in turbulent shear flows using shadowgraphs to visualize the flow field. In particular, among many other interesting features, Brown and Roshko found that large scale coherent structures of the same type existed in a shear layer independent of the value of the Reynolds number provided only that the Reynolds number is large enough to have turbulence. Subsequent studies in other flows, see Roshko¹⁹ for some of the references, have shown that organized structures exist in these flows also. In addition, recent theoretical studies have shown that many of the features of the large scale coherent structures observed in high Reynolds number flows can be described by vortex structures satisfying Euler's equations.

The spatially periodic structures calculated in the starting thermal and the plume have been found to be vortices of alternating sign produced in the heating region and convected out by buoyancy. These vortices increase in strength with height above the floor and occur in anti-symmetric pairs with respect to the centerline of the room. We interpret these structures as analogous to the large scale coherent structures observed in turbulent shear flows. In addition, because these vortices are convected with the buoyant flow, the spatial periodicity is translated into a temporal frequency: at any point within the plume, each of the dependent variables oscillates with a frequency related to the rate at which vortices are generated and convected away. Experiments, both at NBS²⁰ and elsewhere,²¹ have demonstrated qualitatively the same feature; namely, buoyant "puffs", or regular upwellings followed by short quiescent periods, produced at a frequency determined by the experimental arrangement. The frequency of these puffs is also found to agree with the frequency predicted by these calculations.

B. Rectangular Enclosure with Off-Center Heat Source

In Figure 19 contours of constant temperature are shown at dimensionless time 2.0. As in the previous example, these contours mirror the contours of constant volumetric heat addition rate because the velocity field is very small and problem is linear yet at this early time. The heat source is centered along the floor, one quarter of the length of the room from the left wall.

At time 10.0, Figure 20, the isotherms have the same form as in the previous example, Figure 4, at time 10.0. A buoyant bubble pinched at the bottom by the inflow is beginning to rise from the heat source. There appears still to be symmetry about the centerline of the heat source even though the source is not symmetrically placed within the room. At time 13.0 a buoyant thermal has developed, which is asymmetric with the heated fluid expanding more toward the center of the room than toward the wall. Figures 21, 22, 23, and 24 show the thermal rising, growing, hitting the ceiling and spreading. The heated gas flows across the ceiling toward the right in a gravity current while the heated gas at the left moves down the left wall in a fashion similar to that shown in the first example calculation. As before, there are large scale vortex structures in the plume, but because of the placement of the heat source within the room, there is no longer any symmetry.

APPENDIX

Alternate Non-dimensional Variables

Consider the dimensional system of equations (1) and (4) written in the form:

$$\frac{\partial \rho}{\partial t} + u_i \frac{\partial \rho}{\partial x_i} + \rho \left(\frac{\gamma-1}{\gamma} \right) \frac{1}{p_0} \left[Q - \frac{1}{V} \int Q dV \right] = 0$$

$$\rho \frac{\partial u_i}{\partial t} + u_j \frac{\partial u_i}{\partial x_j} + \frac{\partial \tilde{p}}{\partial x_i} + [\rho - \rho_0(y)] g k_i = 0 \quad (A1)$$

$$\frac{\partial u_i}{\partial x_i} = \frac{\gamma-1}{\gamma} \frac{1}{p_0} \left[Q - \frac{1}{V} \int Q dV \right]$$

Here ρ and u_i are the density and velocity components as defined in the text. The quantities $\rho_0(y)$ and \tilde{p} are respectively the initial density stratification in the vertical (y) direction and the difference between the local pressure and the hydrostatic pressure at the height in question. This pressure difference, which affects the fluid motion, is the quantity \tilde{p} defined in Equation (13b) of the text. The heat source Q is prescribed in the form

$$Q = \frac{Q_0 f(t)}{\ell_x \ell_y \ell_z} \frac{1}{\sqrt{\pi}} e^{-(x-x_c)^2 / \ell_x^2 - y / \ell_y} \quad (A2)$$

Note the slight difference in notation from Equation (27b) of the text.

We now seek to introduce non-dimensional variables, denoted with an asterisk (*), that are close to those defined in the text but which reflect the strength of the heat source Q_0 . To this end, we define the following quantities:

$$x_i = \Pi x_i^*; \quad u_i = U u_i^*(x_b^*, t^*)$$

$$t = (H/U) t^*; \quad p = p_a p_0^*(t^*)$$

$$\tilde{P} = \rho_0(o) U^2 p^*(x_k^*, t^*) \quad (A3)$$

$$\rho = \rho_0(o) \{1 + \beta \rho^*(x_k^*, t)\}$$

$$\rho_0(y) = \rho_0(o) \{1 + \beta \rho_0^*(y^*)\}$$

Here, P_a is the undisturbed ambient pressure, $\rho_0(o)$ the ambient density at the floor, and H the height of the enclosure. The reference velocity U and the dimensionless density ratio β are as yet undefined. These two quantities are now determined by requiring that in the Boussinesq limit, when the density ratio $\beta \rightarrow 0$, all non-geometric parameters disappear from the problem. This leads to the following equations for U and β :

$$U^2/g = \beta \quad (A4)$$

$$\beta U/H = Q_0/H^2 \ell_z P_a.$$

This yields a velocity scale which differs from that employed in the text by a $\sqrt{\beta}$, and a dimensionless density ratio given by

$$\beta = \frac{1}{gH} \left\{ (Q_0/\ell_z) (g/P_a) \right\}^{2/3}. \quad (A5)$$

Finally, the equations of motion (A1) become:

$$\frac{\partial \rho^*}{\partial t^*} + u_1^* \frac{\partial \rho^*}{\partial x_1^*} + (1 + \beta \rho^*) D^* = 0$$

$$(1 + \beta \rho^*) \left(\frac{\partial u_1^*}{\partial t^*} + u_k^* \frac{\partial u_1^*}{\partial x_k^*} \right) + \frac{\partial p^*}{\partial x_1^*} + k_1(\rho^* - \rho_0^*) = 0$$

$$\frac{\partial u_i^*}{\partial x_i^*} = \beta D^* \quad (A6)$$

$$D^* = \frac{\gamma-1}{\gamma} \frac{1}{p_0^*} \left[Q^* - \frac{H^2 \ell_z}{V} f(t^*) \right]$$

$$Q^* = \frac{f(t^*)}{\sqrt{\pi}} \frac{H^2}{\ell_x \ell_y} \exp \left[- \left(\frac{H}{\ell_x} \right)^2 (x^* - x_c^*)^2 - \left(\frac{H}{\ell_y} \right) y^* \right].$$

Note that when β is $O(1)$; i.e., when there are significant density variations, the non-dimensionalization is for all practical purposes the same as that used in the text. The most significant feature of this derivation is Equation (A5) which determines β , and hence the conditions under which a non-Boussinesq model is necessary.

REFERENCES

1. Rehm, R. G. and Baum, H. R., The Equations of Motion for Thermally Driven, Buoyant Flows, J. Research of the National Bureau of Standards 83, No. 3, pp. 297-308 (May-June 1978).
2. Batchelor, G. K., The Conditions for Dynamical Similarity of Motions of a Frictionless Perfect-Gas Atmosphere, Quart. J. Roy. Meteor. Soc. 79, pp. 224-235 (1953).
3. Quintiere, J., Growth of Fire in Building Compartments, Fire Standards and Safety, Ed. A. F. Robertson, ASTM STP 614, pp. 131-167 (American Society for Testing and Materials, New York, NY, 1977).
4. Porsching, T. A., A Finite Difference Method for Thermally Expandable Fluid Transients, Nuclear Sci. and Eng. 64, pp. 177-186 (Sept. 1977).
5. Roache, P. J., Computational Fluid Dynamics, Hermosa Publishers, P. O. Box 8172, Albuquerque, NM 87108.
6. Lamb, H., Hydrodynamics, Sixth Edition, Dover Publications, New York, pp. 378-380 (1932); also,

Prandtl, L., Essentials of Fluid Dynamics, Blackie and Son Ltd., London, pp. 374-377 (1952).
7. Turner, J. S., Buoyancy Effects in Fluids, Cambridge University Press, Chapter 2 (1973); also,

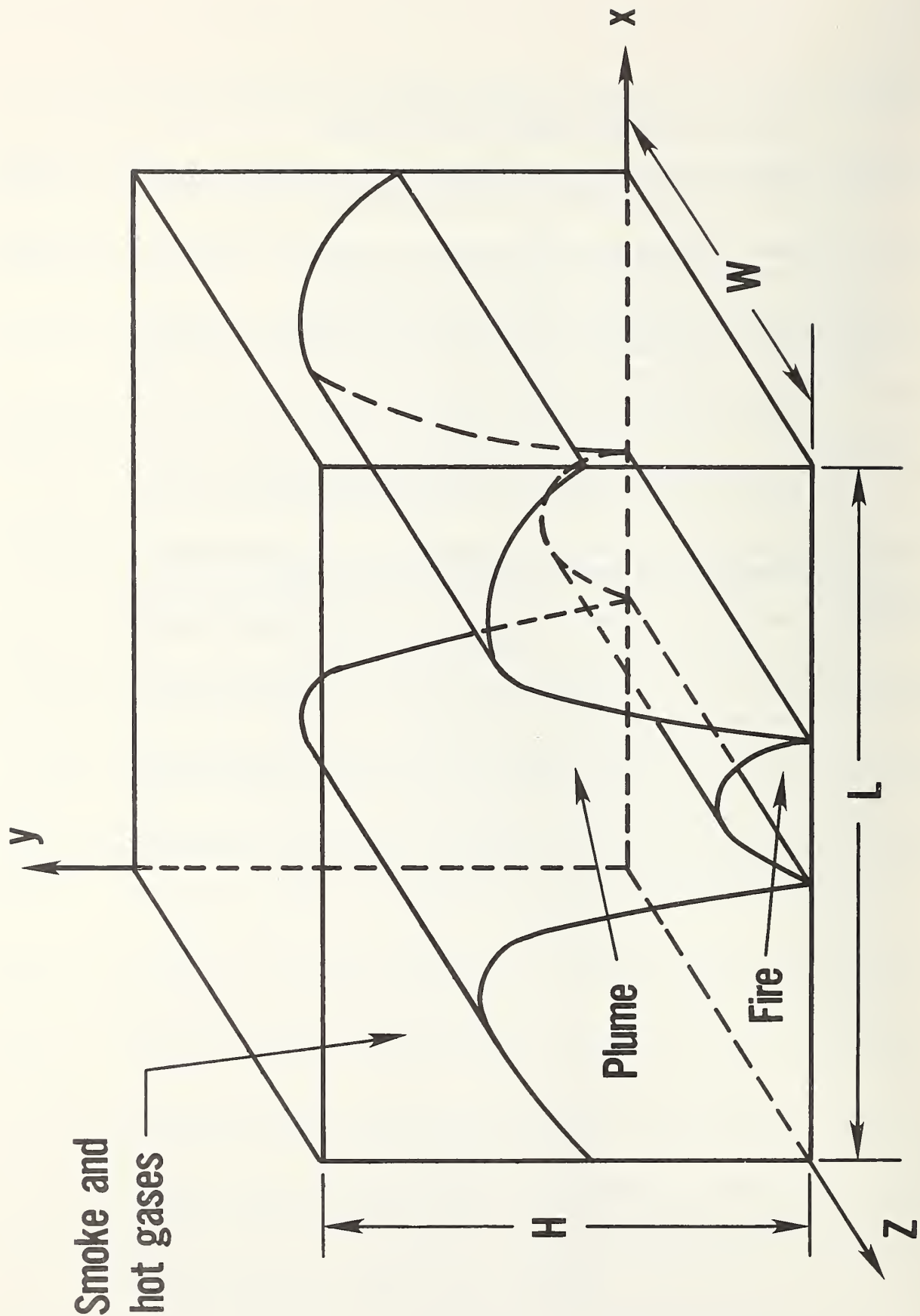
Whitham, G. B., Linear and Nonlinear Waves, John Wiley and Sons, New York, pp. 421-423 (1974).
8. Baum, H. R. and Rehm, R. G., Finite Difference Solutions for Internal Waves in Enclosures, National Bureau of Standards Report in preparation.
9. Arakawa, A., Computational Design for Long-Term Numerical Integration of the Equations of Fluid Motion: Two-Dimensional Incompressible Flow. Part I, J. Comp. Phys. 1, pp. 119-143 (1966).
10. Phillips, N. A., "An Example of Non-Linear Computational Instability," The Atmosphere and Sea in Motion, pp. 501-504, Rockefeller Inst. Press in association with Oxford University Press (1959).
11. Arakawa, A. and Lamb, V. R., Computational Design of the Basic Dynamical Processes of the UCLA General Circulation Model, Methods in Computational Physics, Vol. 17 General Circulation Models of the Atmosphere, J. Chang (ed.), Academic Press, New York, pp. 173-265 (1977).
12. Harlow, F. H. and Amsden, A. A., Fluid Dynamics, A LASL Monograph, Los Alamos Scientific Laboratory Report LA4700, Los Alamos, New Mexico (June 1971).

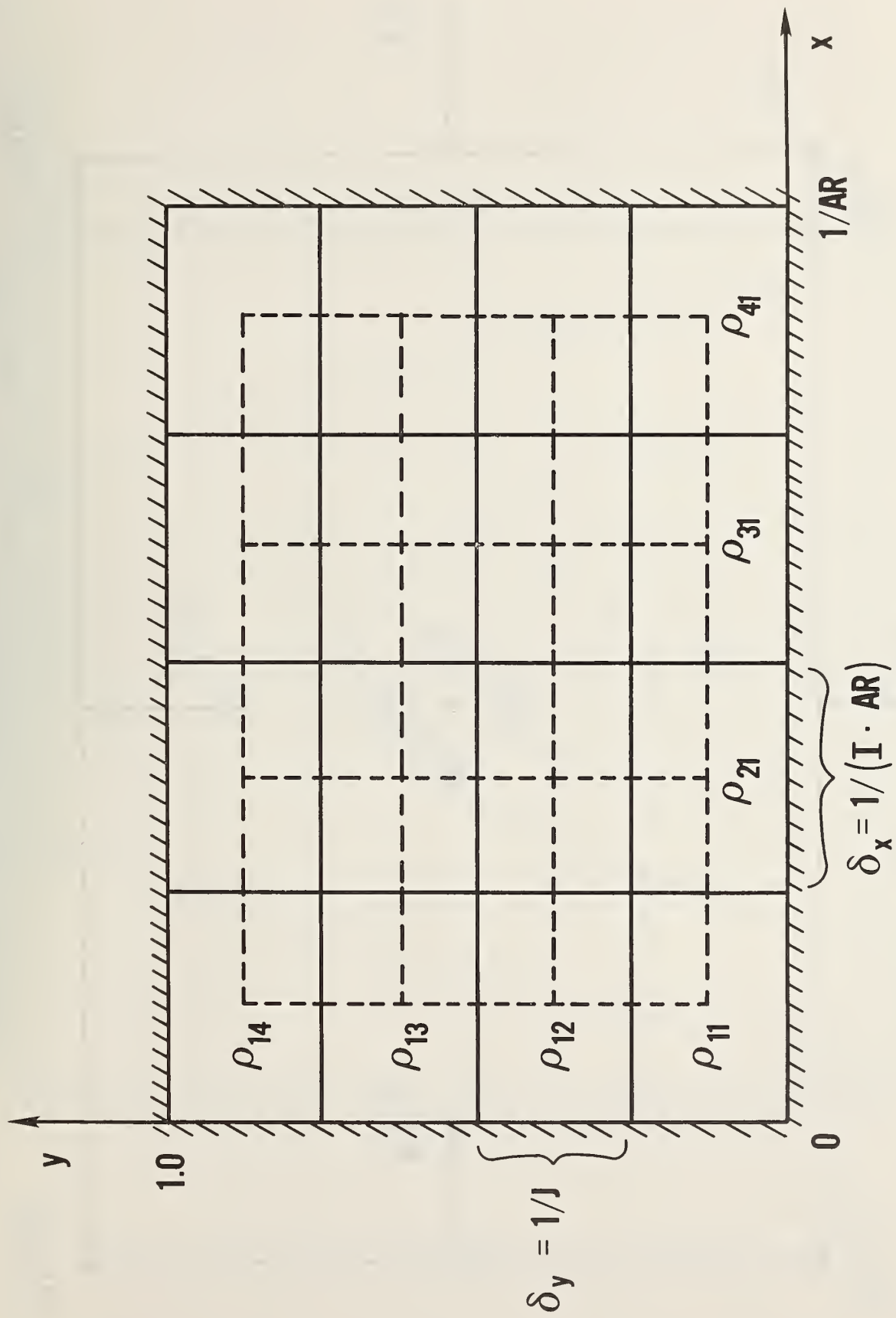
13. Kreiss, H. and Oliger, J., Methods for the Approximate Solution of Time Dependent Problems, Global Atmospheric Research Programme (GARP) Publication Series No. 10, February 1973.
14. Schwarztrauber, P. and Sweet, R., Efficient FORTRAN Subprograms for the Solution of Elliptic Partial Differential Equations, NCAR-TN/IA-109, July (1975).
15. Concus, P. and Golub, G., Use of Fast Direct Methods for the Efficient Numerical Solution of Nonseparable Elliptic Equation, SIAM J. Numer. Anal., 10, 6 (Dec. 1973).
16. Concus, P., Golub, G., and O'Leary, D. P., A Generalized Conjugate Gradient Method for the Numerical Solution of Elliptic Partial Differential Equations, in Sparse Matrix Computations, J. Bunch & D. Rose, ed., pp. 309-332, Academic Press, New York (1976).
17. Lewis, J. and Rehm, R. G., The Numerical Solution of a Nonseparable Elliptic Partial Differential Equation by Preconditioned Conjugate Gradients, NBS Journal of Research, 85, No. 5, pp. 367-390 (September-October 1980).
18. Brown, G. L. and Roshko, A., On Density Effects and Large Structure in Turbulent Mixing Layers, Journal of Fluid Mechanics, Vol. 64, pp. 775-816 (1974).
19. Roshko, A., Structure of Turbulent Shear Flows: A New Look, AIAA Journal, Vol. 14, No. 10, pp. 1349-1357 (October 1976).
20. McCaffrey, B., Purely Buoyant Diffusion Flames: Some Experimental Results, National Bureau of Standards Report NBSIR 79-1910 (October, 1979).
21. Zukowski, E., Kubota, T. and Cetegen, B., Entrainment in Fire Plumes, Fire Safety Journal 3, pp. 107-121 (1980/81).
22. Rehm, R. G., Baum, H. R., Corley, D. M. and Barnett, P. D., Finite Difference Calculations of Buoyant Convection in an Enclosure, Part II: Verification of the Basic Algorithm, National Bureau of Standards Report in preparation.

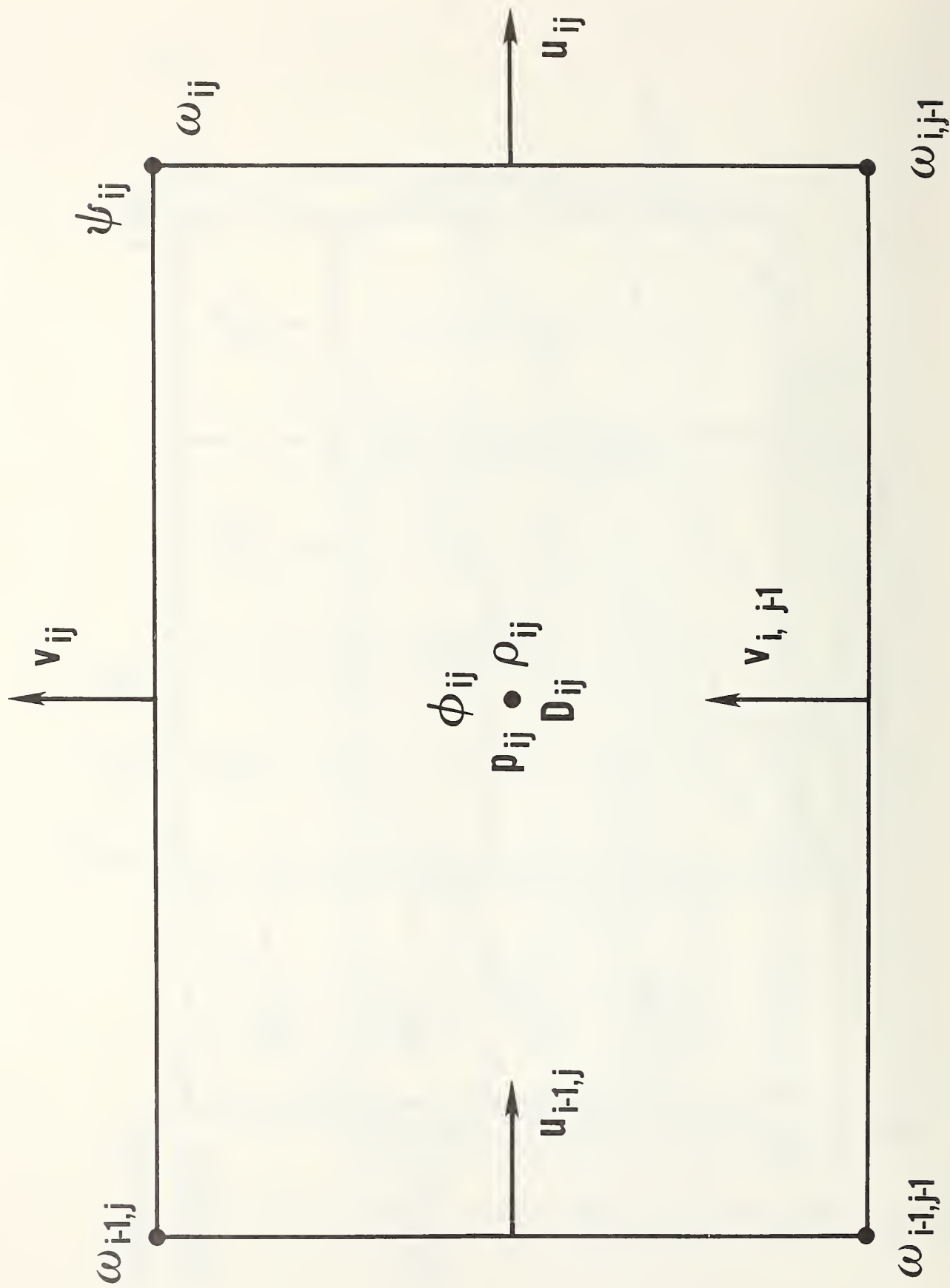
Figure Captions

- Figure 1 Schematic diagram of an enclosure with a two-dimensional heat source, plume and region of smoke and hot gases.
- Figure 2a Rectangular enclosure in dimensionless variables $0 \leq x \leq \frac{1}{AR}$, $0 \leq y \leq 1$. The mesh upon which the difference scheme is based as shown schematically for $(I = J = 4)$ as a grid of solid lines. The mesh of dashed lines joins the center points of the basic mesh cells and is the grid upon which the pressure computation is performed.
- Figure 2b A typical mesh cell, with center located at $x = (i - 1/2) \delta x$ and $y = (j - 1/2) \delta y$, illustrating where all dependent variables for the finite difference scheme are defined.
- Figure 3 Contours of constant temperature at dimensionless time $t = 2.0$ in a square enclosure using a 31×31 mesh. At this early time convection is unimportant, and isotherms reflect contours of constant volumetric heat addition.
- Figure 4 Contours of constant temperature at dimensionless time $t = 10.0$ in a square enclosure using a 31×31 mesh.
- Figure 5 Contours of constant temperature at dimensionless time $t = 11.5$ in a square enclosure using a 31×31 mesh.
- Figure 6 Contours of constant temperature at dimensionless time $t = 12.5$ in a square enclosure using a 31×31 mesh.
- Figure 7 Contours of constant temperature at dimensionless time $t = 13.5$ in a square enclosure using a 31×31 mesh.
- Figure 8 Contours of constant temperature at dimensionless time $t = 14.5$ in a square enclosure using a 31×31 mesh.
- Figure 9 Contours of constant temperature at dimensionless time $t = 15.5$ in a square enclosure using a 31×31 mesh.
- Figure 10 Contours of constant temperature at dimensionless time $t = 16.5$ in a square enclosure using a 31×31 mesh.
- Figure 11 Contours of constant temperature at dimensionless time $t = 17.5$ in a square enclosure using a 31×31 mesh.
- Figure 12 Contours of constant temperature at dimensionless time $t = 18.5$ in a square enclosure using a 31×31 mesh.
- Figure 13 Contours of constant temperature at dimensionless time $t = 2.0$ in a square enclosure using a 63×64 mesh.

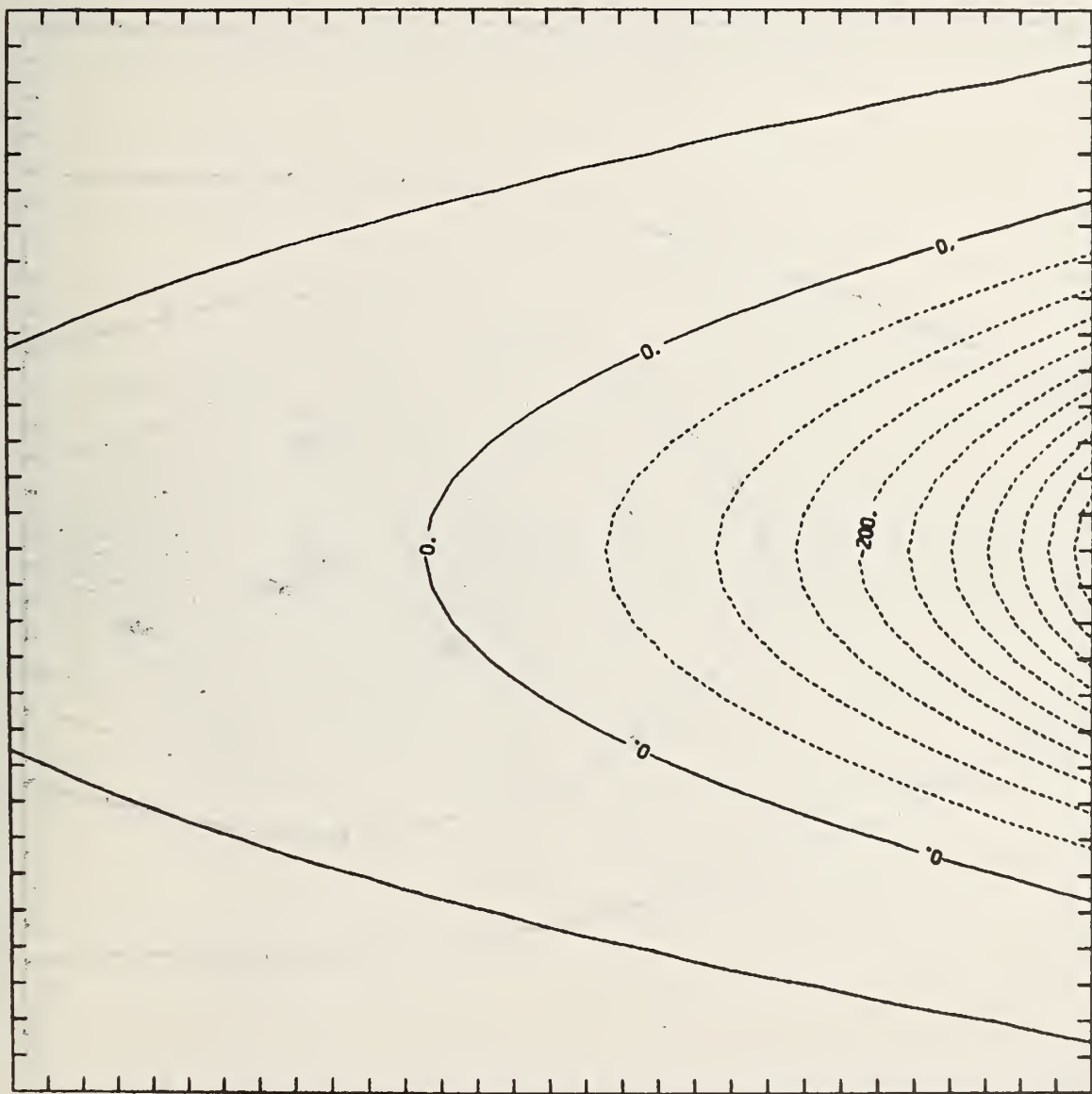
- Figure 14 Contours of constant temperature at dimensionless time $t = 10.0$ in a square enclosure using a 63×64 mesh.
- Figure 15 Contours of constant temperature at dimensionless time $t = 11.225$ in a square enclosure using a 63×64 mesh.
- Figure 16 Contours of constant temperature at dimensionless time $t = 13.225$ in a square enclosure using a 63×64 mesh.
- Figure 17 Contours of constant temperature at dimensionless time $t = 15.225$ in a square enclosure using a 63×64 mesh.
- Figure 18 Contours of constant temperature at dimensionless time $t = 16.187$ in a square enclosure using a 63×64 mesh.
- Figure 19 Contours of constant temperature at dimensionless time $t = 2.0$ in a rectangular enclosure using a 62×31 mesh.
- Figure 20 Contours of constant temperature at dimensionless time $t = 10.0$ in a rectangular enclosure using a 62×31 mesh.
- Figure 21 Contours of constant temperature at dimensionless time $t = 13.0$ in a rectangular enclosure using a 62×31 mesh.
- Figure 22 Contours of constant temperature at dimensionless time $t = 15.45$ in a rectangular enclosure using a 62×31 mesh.
- Figure 23 Contours of constant temperature at dimensionless time $t = 17.95$ in a rectangular enclosure using a 62×31 mesh.
- Figure 24 Contours of constant temperature at dimensionless time $t = 20.45$ in a rectangular enclosure using a 62×31 mesh.



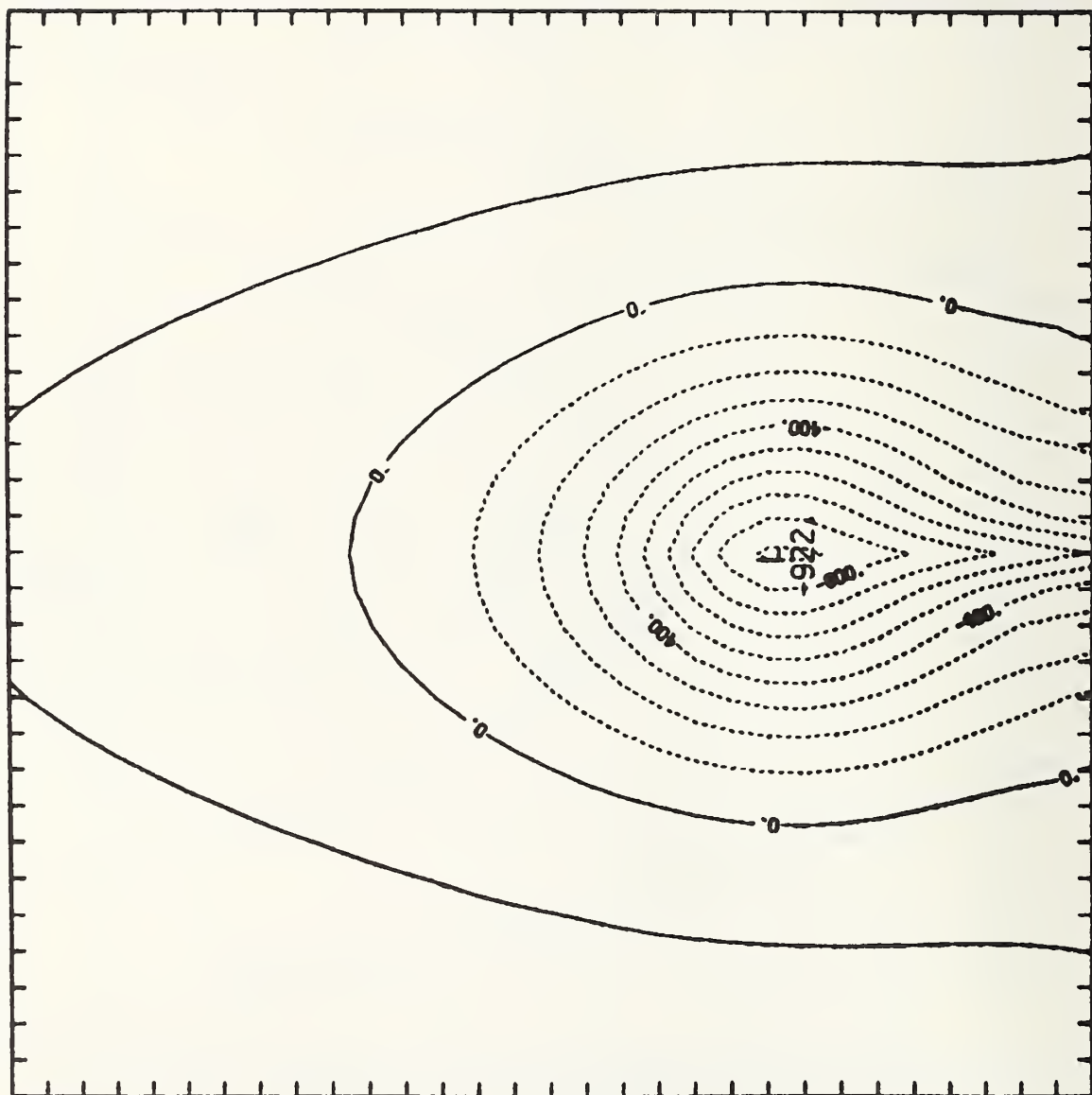




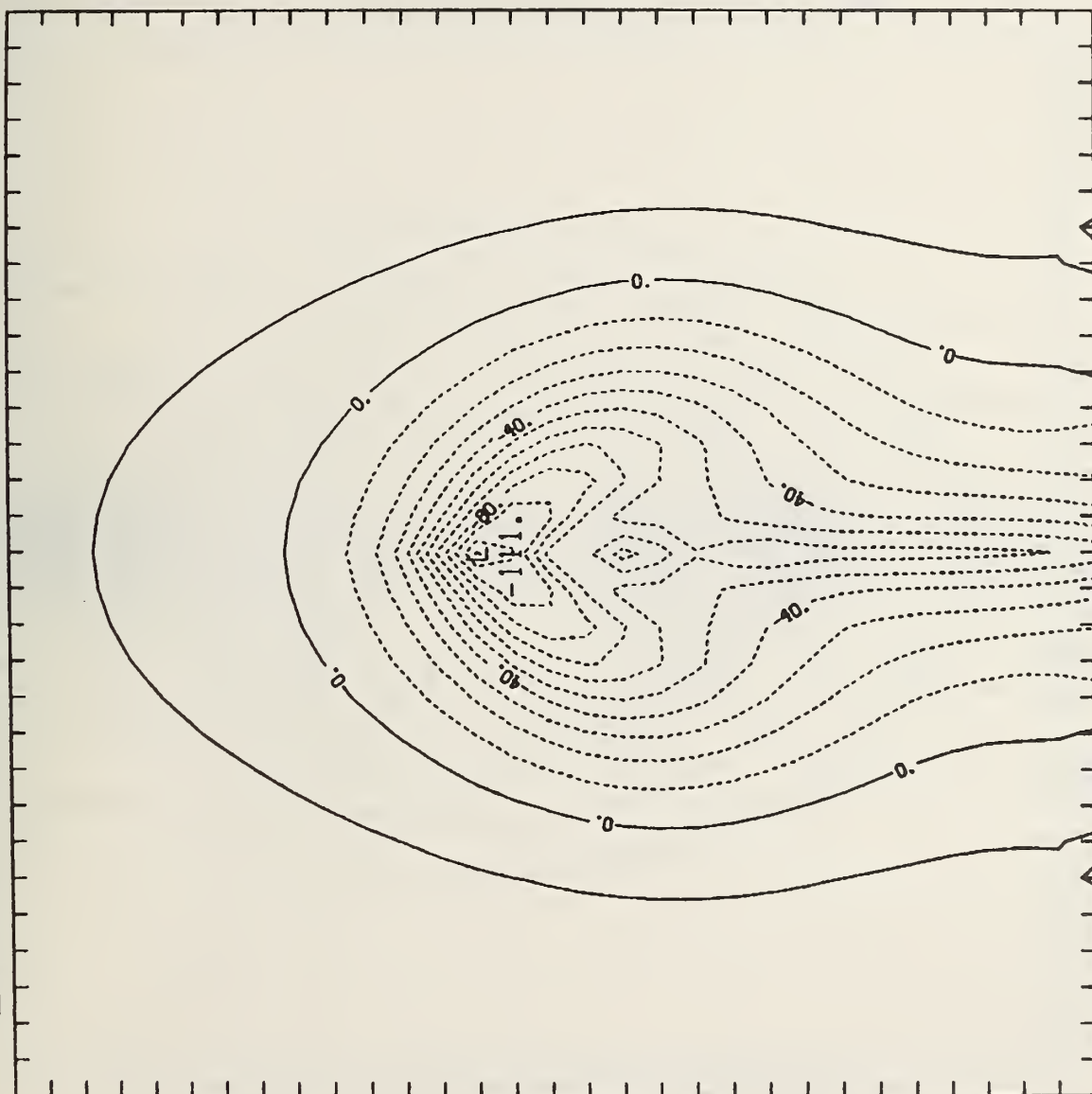
TEMPERATURE CØNTØRS AT T = 2.000



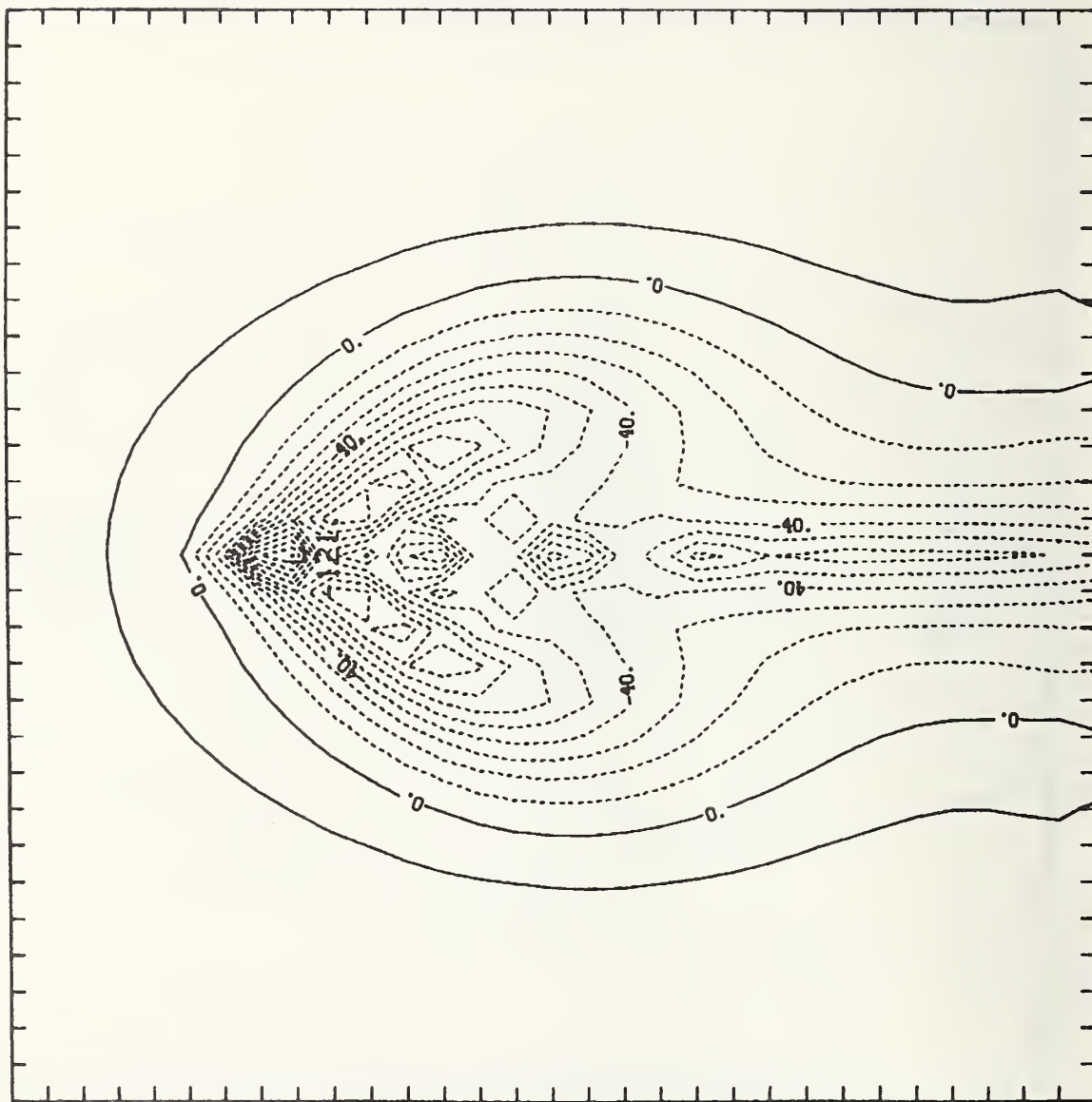
TEMPERATURE CØNTØRS AT T = 10.000



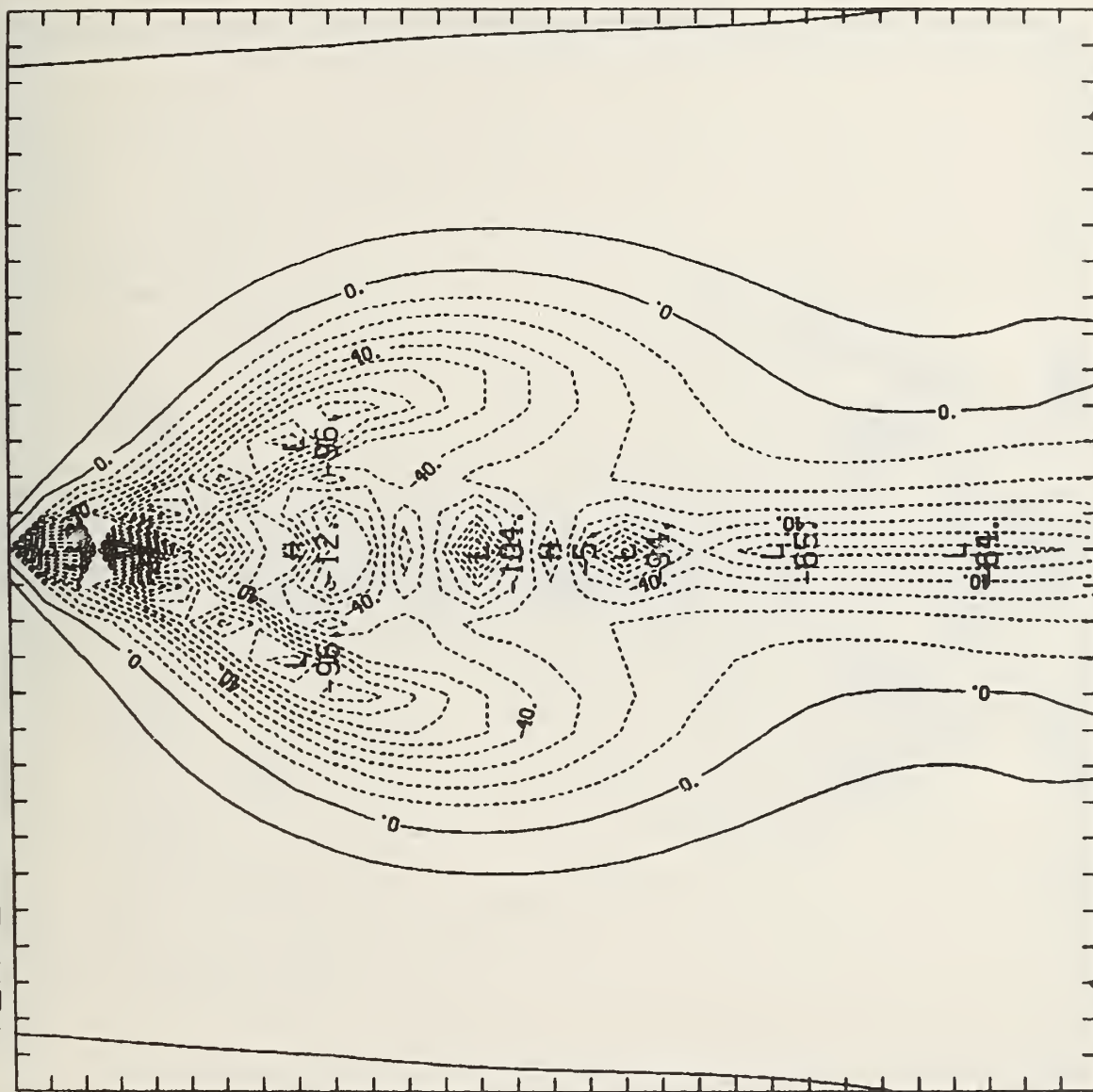
TEMPERATURE CØNTØRS AT T = 11.500



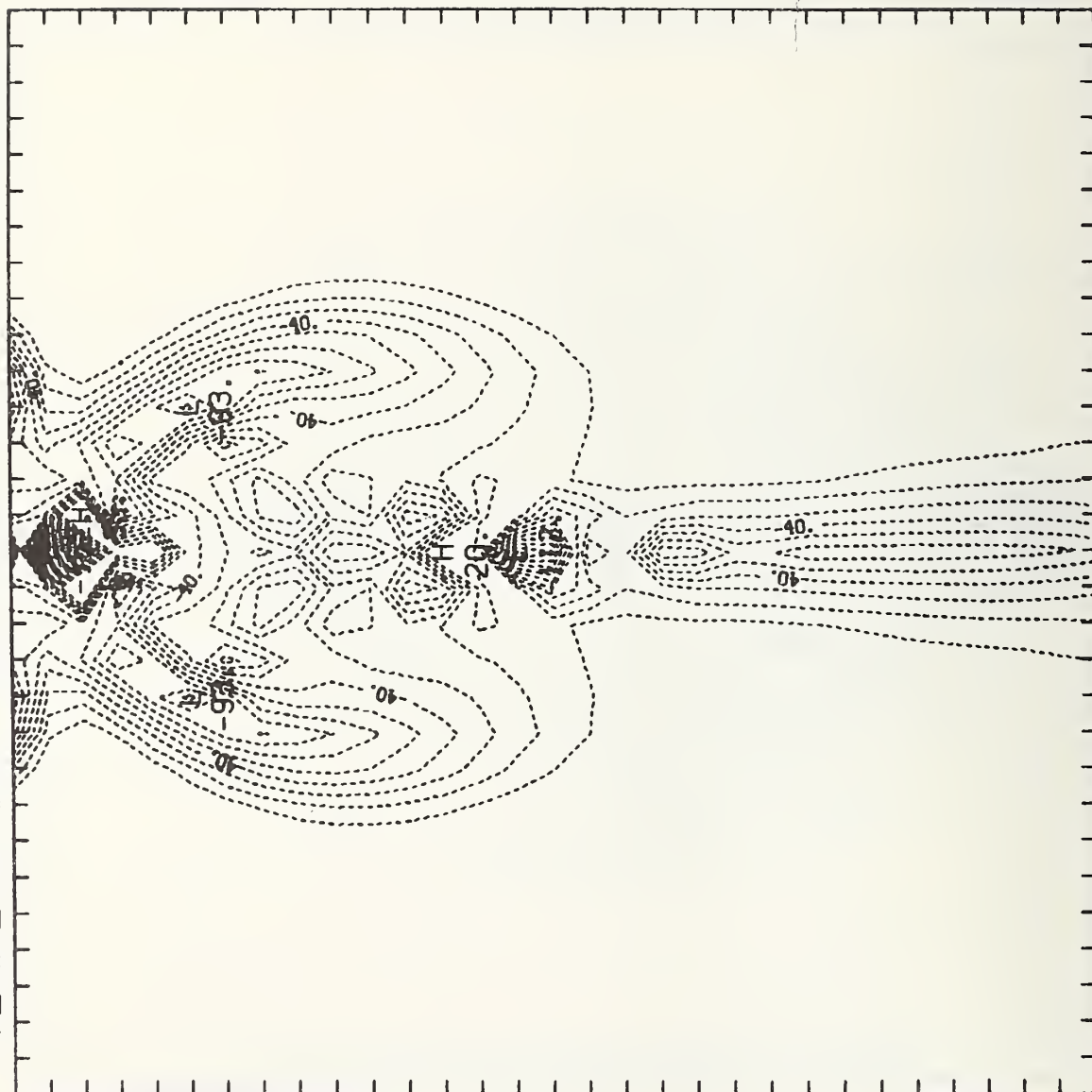
TEMPERATURE CØNTØURS AT T = 12.500



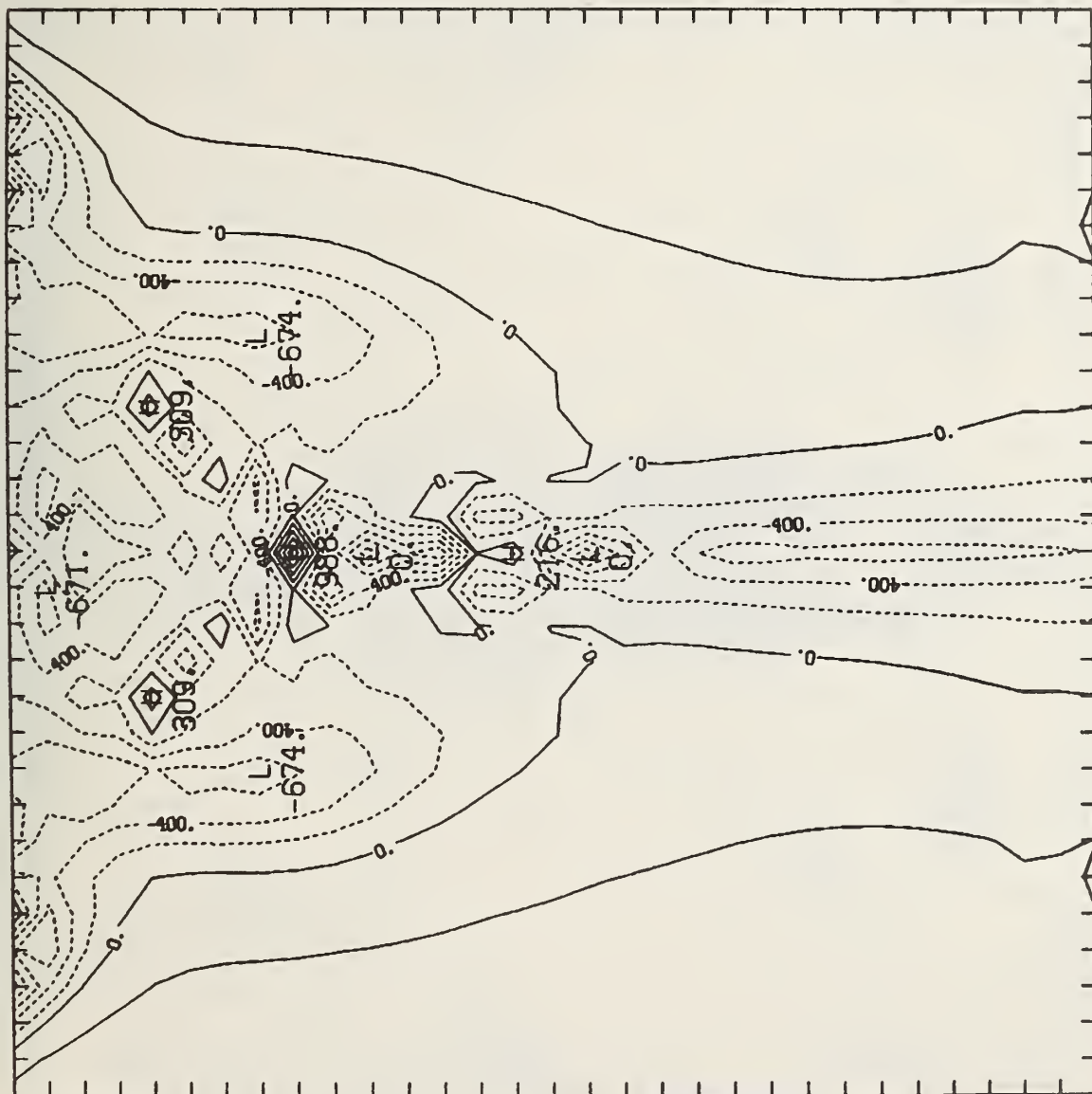
TEMPERATURE CØNTØURS AT T = 13.500



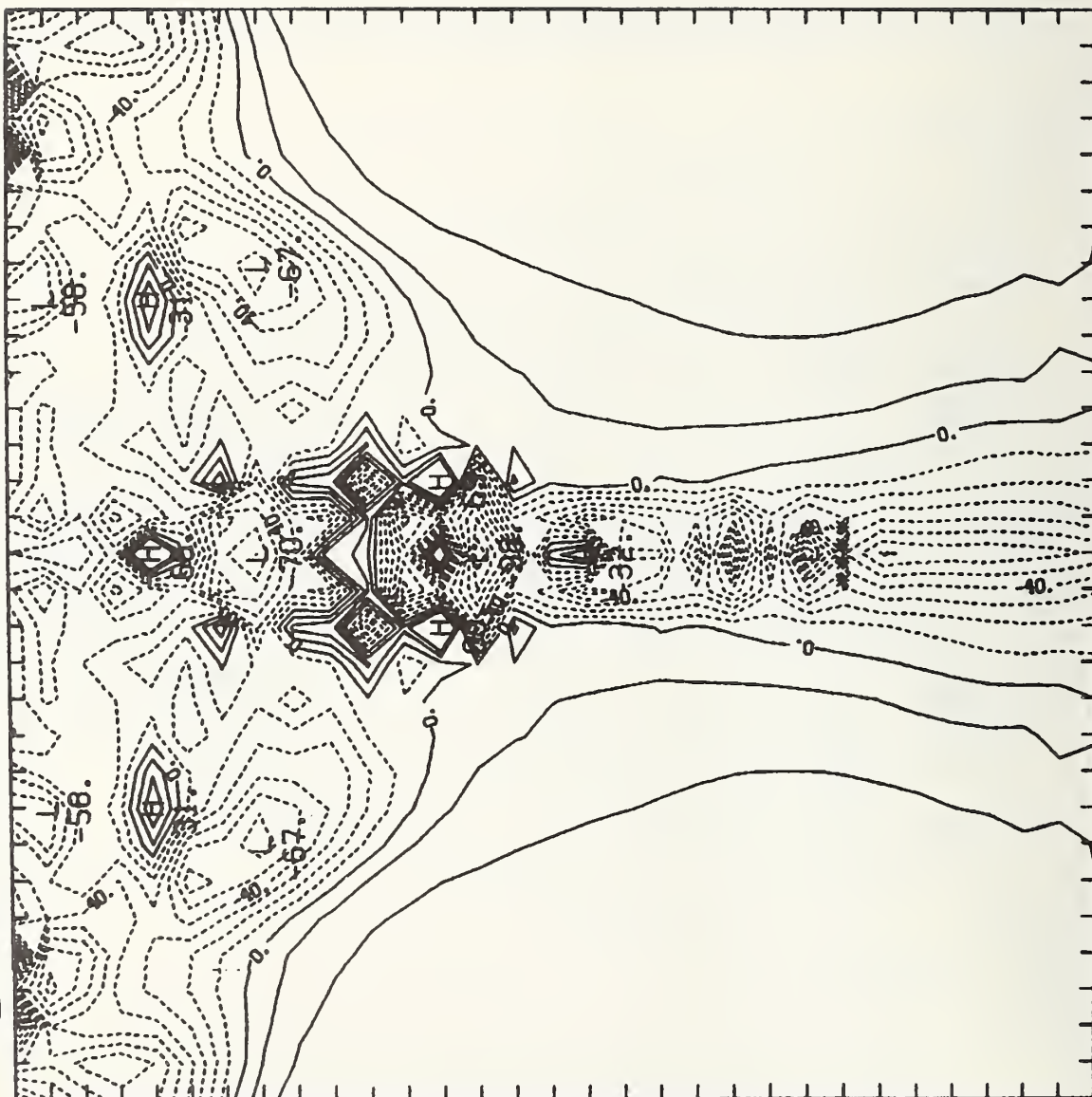
TEMPERATURE CØNTØURS AT T = 14.500



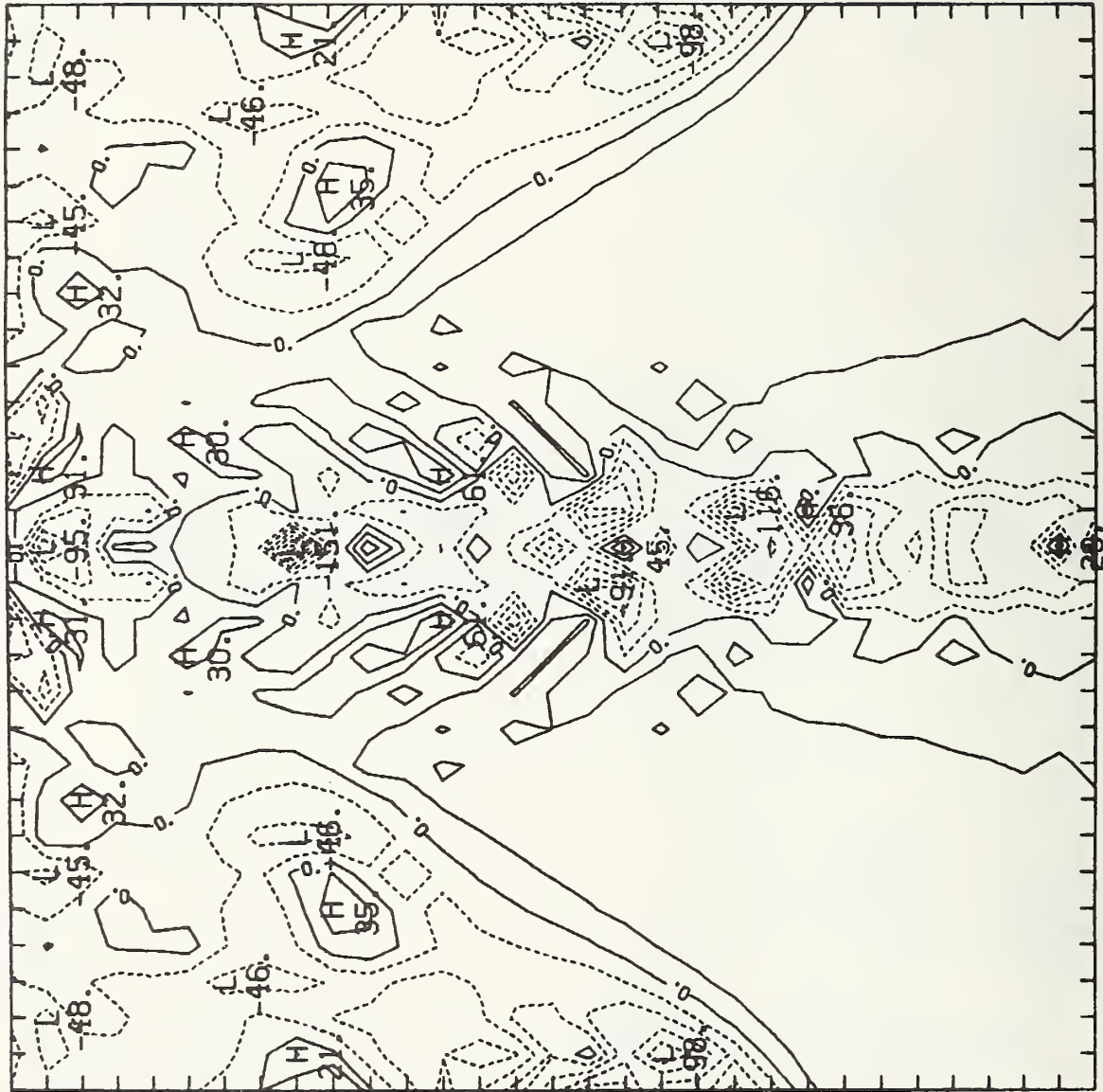
TEMPERATURE CØNTØRS AT T = 15.500



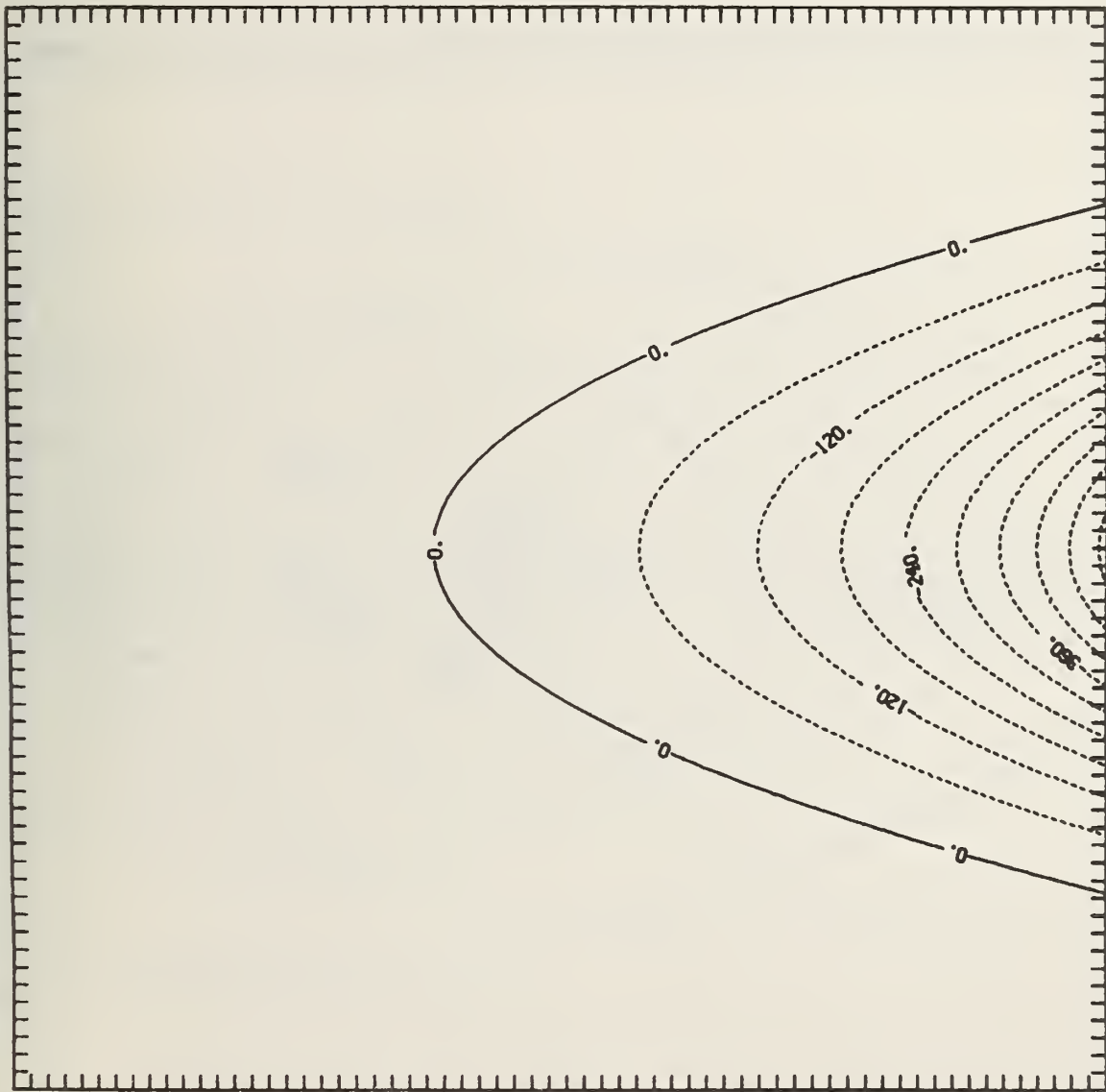
TEMPERATURE CØNTØURS AT T = 16.500



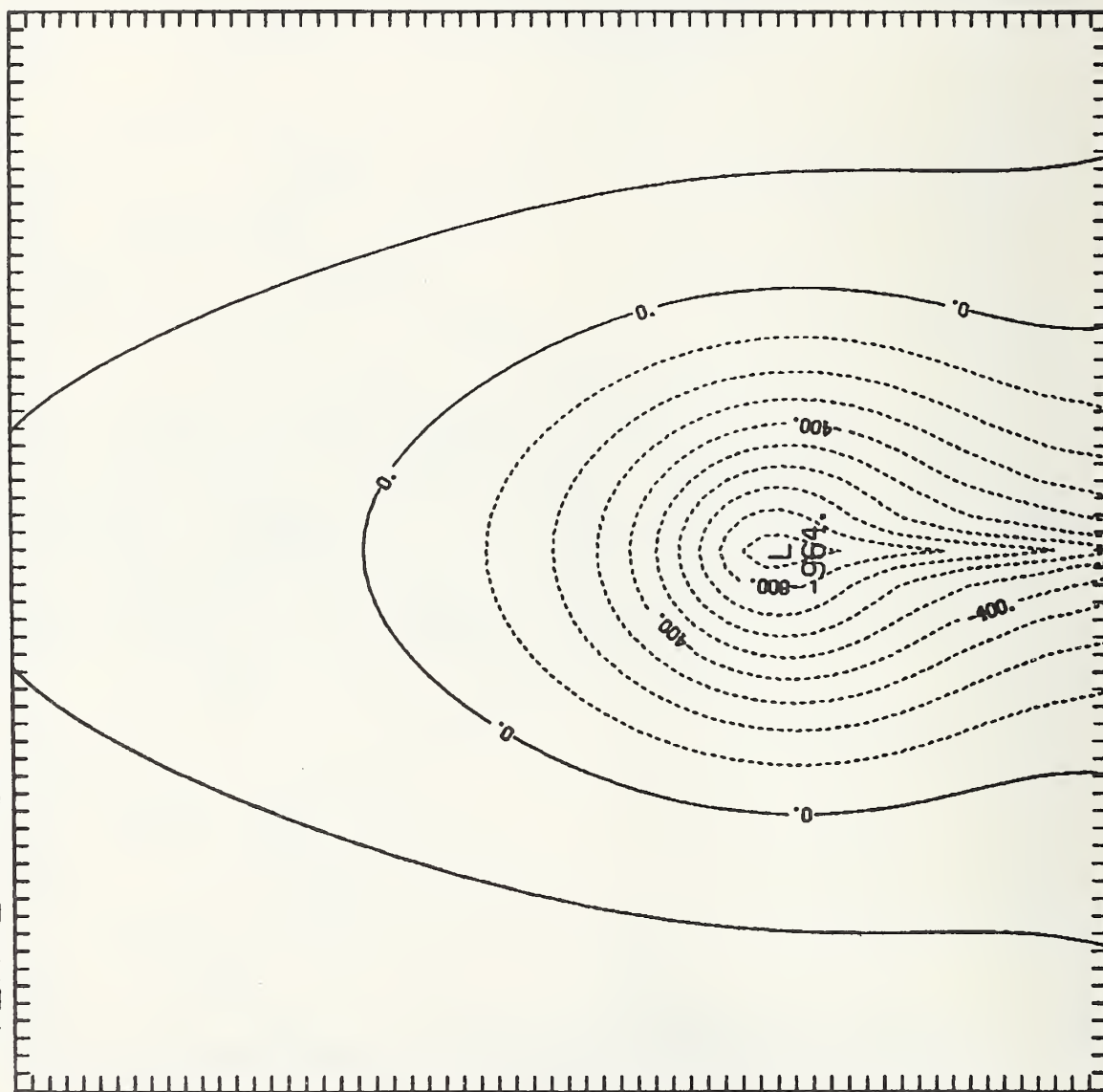
TEMPERATURE CØNTØURS AT T = 18.500



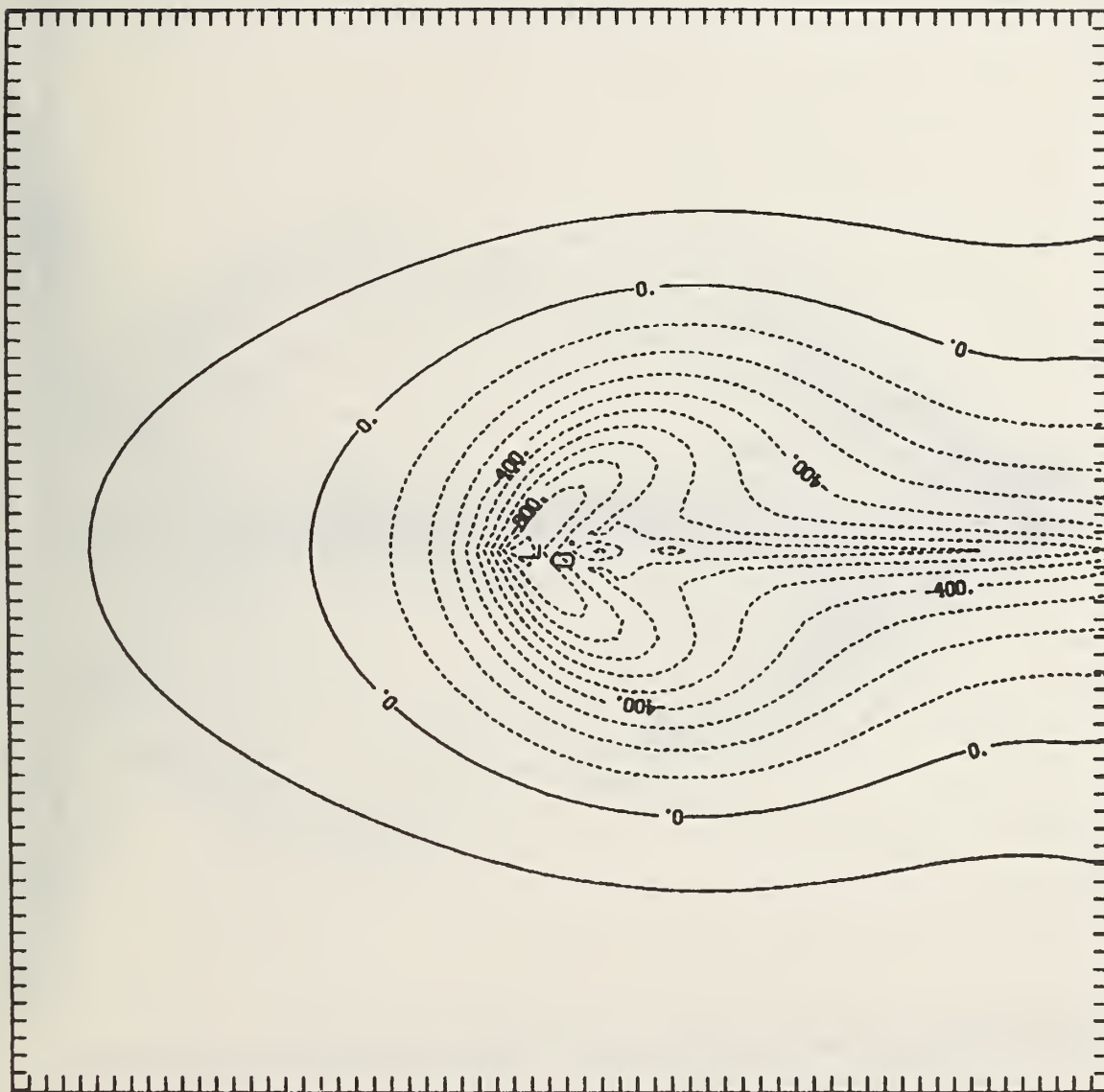
TEMPERATURE CØNTØURS AT T = 2.000



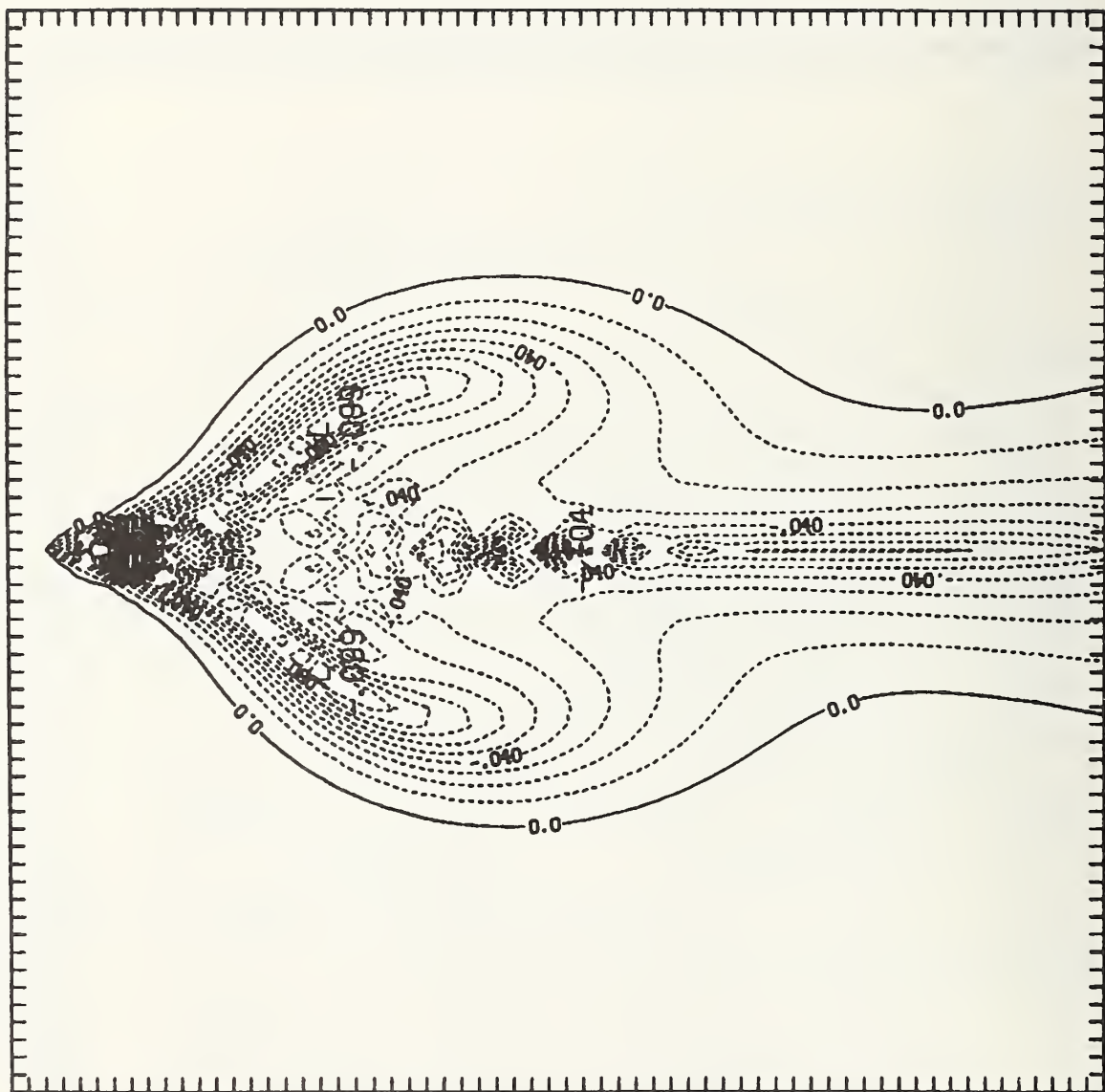
TEMPERATURE CØNTØURS AT T = 10.000



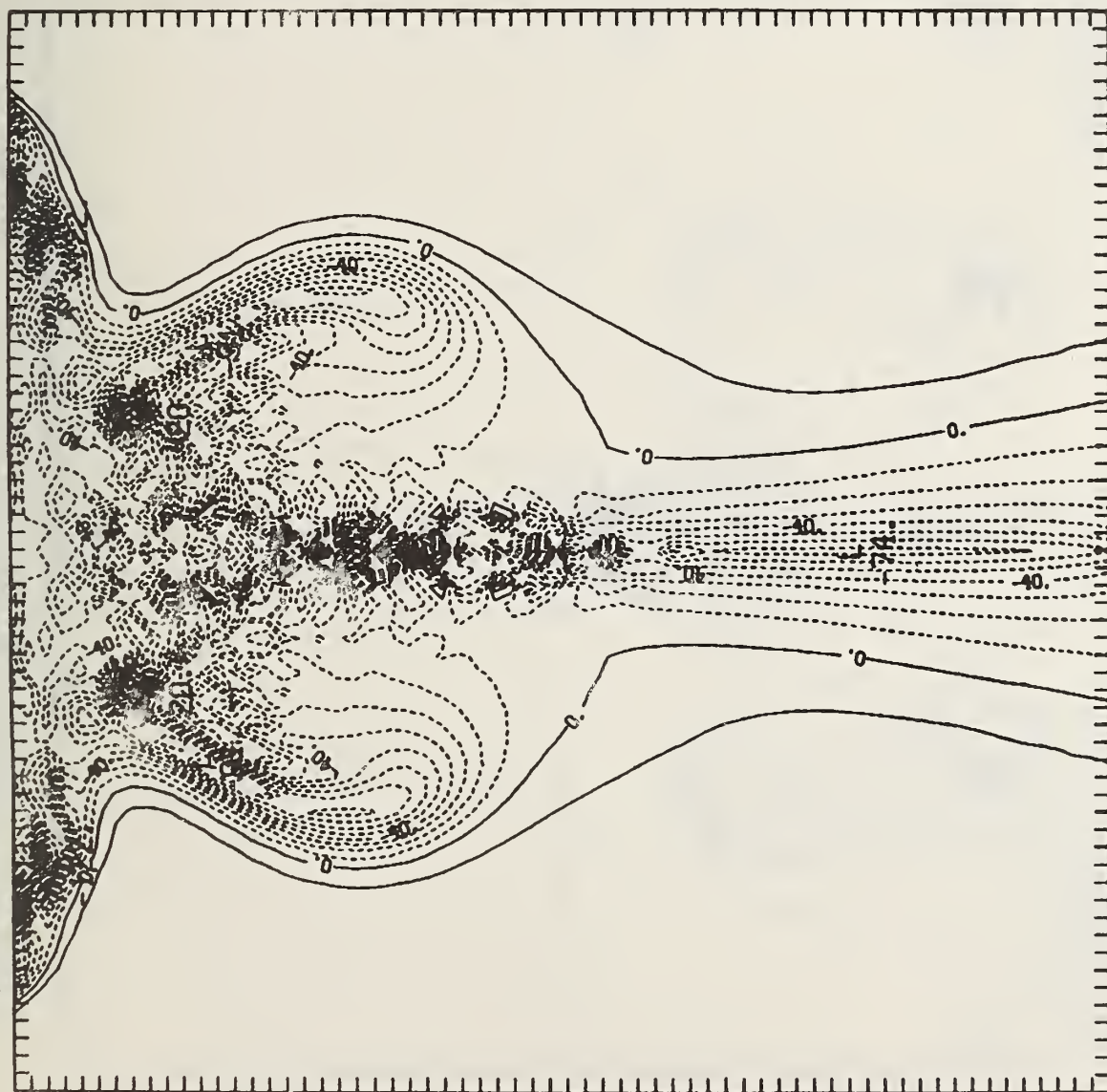
TEMPERATURE CØNTØURS AT T = 11.225



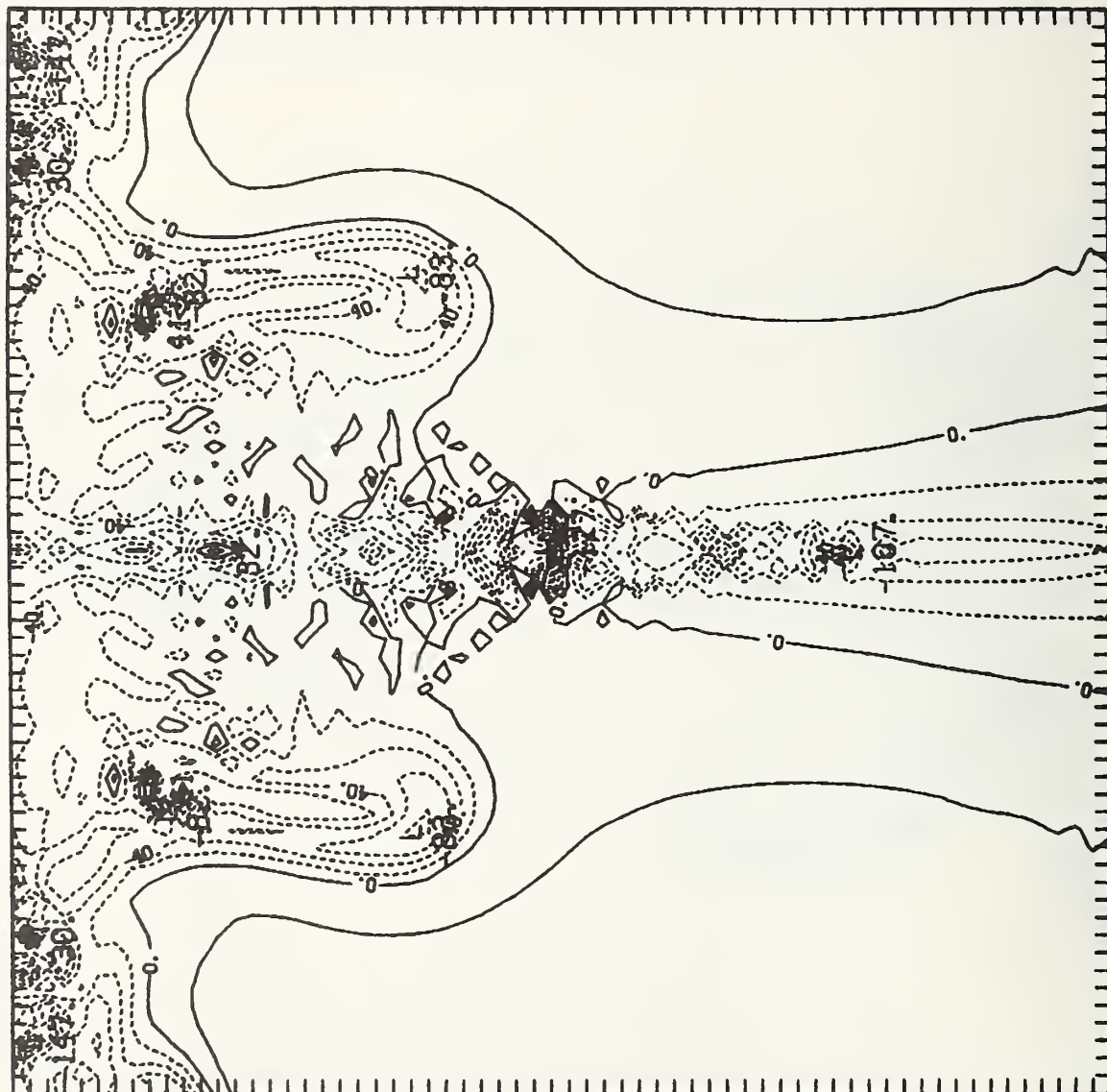
TEMPERATURE CØNTØRS AT T = 13.225



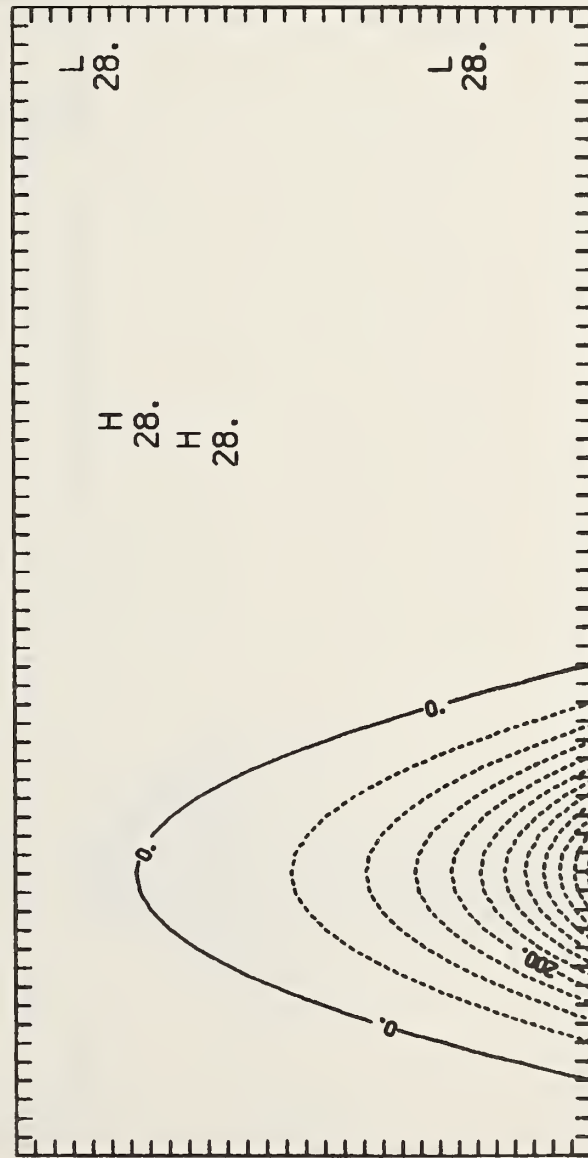
TEMPERATURE CØNTØURS AT T = 15.225



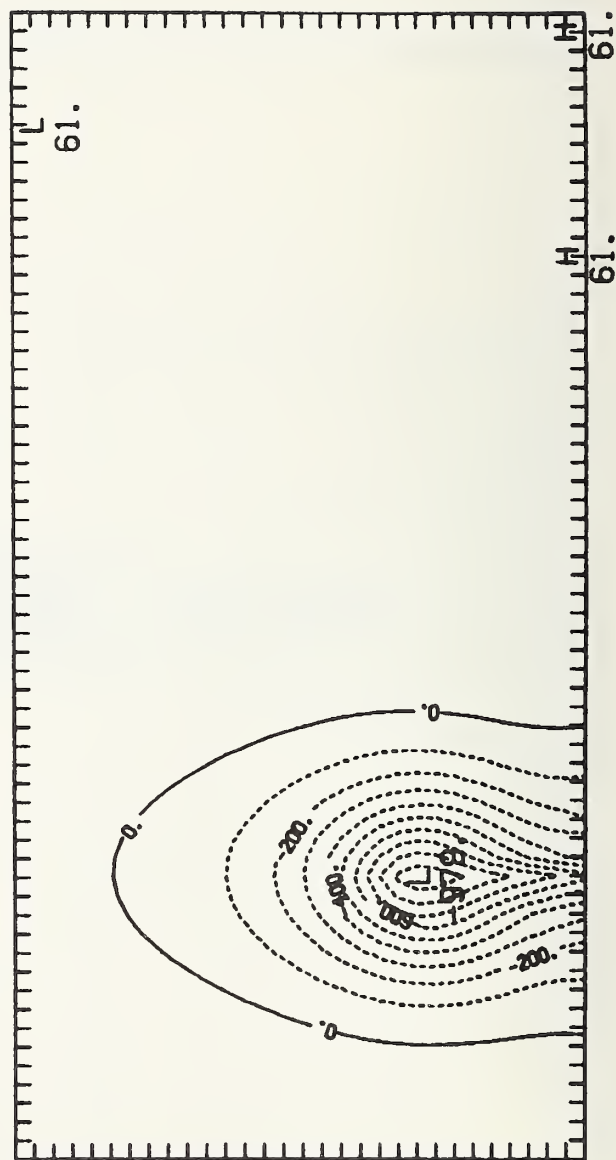
TEMPERATURE CØNTØRS AT T = 16.187



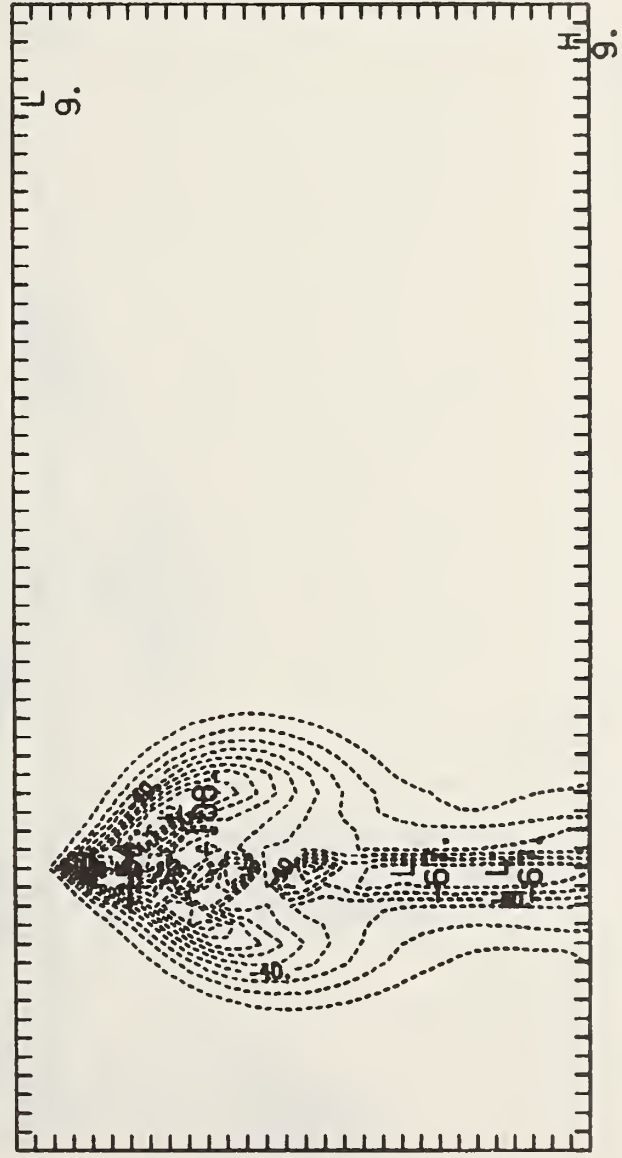
TEMPERATURE CØNTØURS AT T = 2.000



TEMPERATURE CØNTØURS AT $T = 10.000$



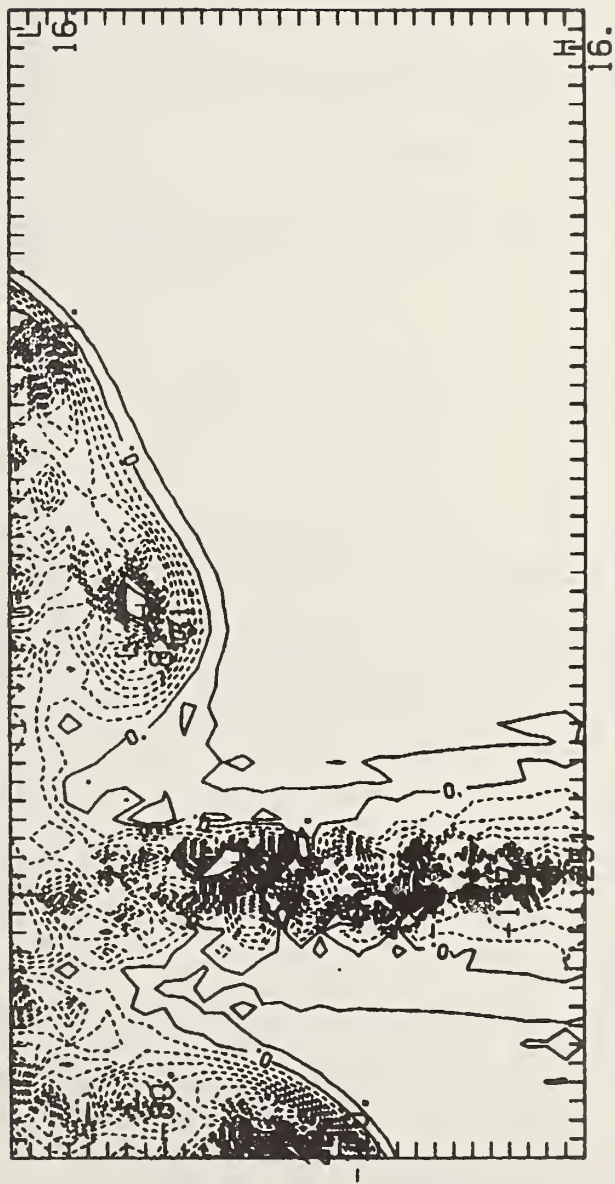
TEMPERATURE CØTØURS AT T = 13.000



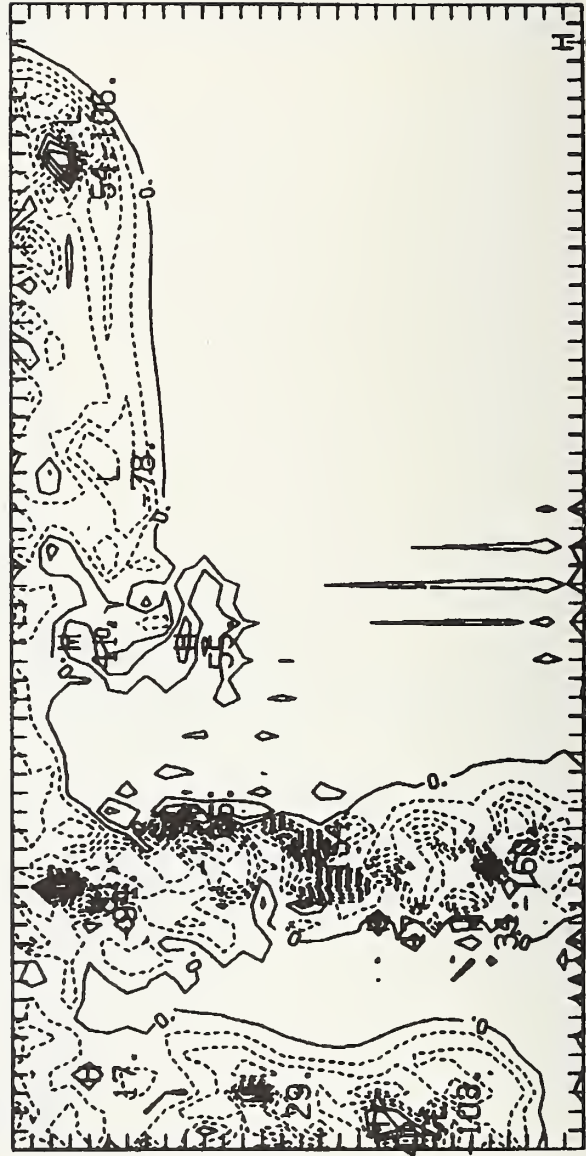
TEMPERATURE CØNTØURS AT T = 15.450



TEMPERATURE CØNTØURS AT T = 17.950



TEMPERATURE CØNTØURS AT T = 20.450



U.S. DEPT. OF COMM. BIBLIOGRAPHIC DATA SHEET (See instructions)	1. PUBLICATION OR REPORT NO. NBSIR 81-2385 (NBS)	2. Performing Organ. Report No.	3. Publication Date December, 1981
4. TITLE AND SUBTITLE Finite Difference Calculation of Buoyant Convection in an Enclosure Part I: The Basic Algorithm			
5. AUTHOR(S) Howard R. Baum, Ronald G. Rehm, P. Darcy Barnett and Daniel M. Corley			
6. PERFORMING ORGANIZATION (If joint or other than NBS, see instructions) NATIONAL BUREAU OF STANDARDS DEPARTMENT OF COMMERCE WASHINGTON, D.C. 20234		7. Contract/Grant No.	8. Type of Report & Period Covered Final
9. SPONSORING ORGANIZATION NAME AND COMPLETE ADDRESS (Street, City, State, ZIP) Center for Applied Mathematics National Engineering Laboratory National Bureau of Standards			
10. SUPPLEMENTARY NOTES <input type="checkbox"/> Document describes a computer program; SF-185, FIPS Software Summary, is attached.			
11. ABSTRACT (A 200-word or less factual summary of most significant information. If document includes a significant bibliography or literature survey, mention it here) A novel mathematical model of buoyant convection in an enclosure, developed earlier, is solved by finite difference techniques in the two-dimensional case. This model has been developed as a principal analytical tool for the prediction of the movement of smoke and not gases in fires. Effects of large density variations caused by substantial heating are retained while acoustic (high-frequency) waves, which are unimportant to buoyant convection, are analytically filtered out. No viscous or thermal conduction effects are included in the model. These two characteristics (filtering and no dissipative effects) distinguish the model from all others describing buoyant convection. The mathematical model consists of a mixed hyperbolic and elliptic set of non-linear partial differential equations: the problem is a mixed initial, boundary value one. An explicit time-marching algorithm, second-order accurate in both space and time, is used to solve the equations. The computational procedure uses a software package for solving a nonseparable elliptic equation developed especially for this problem. The finite difference solutions have been carefully compared with analytical solutions obtained in special cases to determine the stability and accuracy of the numerical solutions. The computer model has been used to compute the buoyant convection produced in an enclosure by a spatially distributed heat source simulating a fire. The computed results show qualitative agreement with experimentally observed buoyant convection in enclosure fires.			
12. KEY WORDS (Six to twelve entries; alphabetical order; capitalize only proper names; and separate key words by semicolons) buoyant convection; computations-finite difference; Euler equations; finite difference equations; fire-enclosure; fluid flow; heat source-volumetric; partial differential equations			
13. AVAILABILITY <input checked="" type="checkbox"/> Unlimited <input type="checkbox"/> For Official Distribution. Do Not Release to NTIS <input type="checkbox"/> Order From Superintendent of Documents, U.S. Government Printing Office, Washington, D.C. 20402. <input checked="" type="checkbox"/> Order From National Technical Information Service (NTIS), Springfield, VA. 22161		14. NO. OF PRINTED PAGES 67 15. Price \$8.00	

